Spatio-Temporal Characteristics and Driving Mechanism of Alpine Peatland InSAR Surface Deformation—A Case Study of Maduo County, China

Yaoxiang Liu, Yi He, Wang Yang, and Lifeng Zhang

***Abstract*—Surface deformation of alpine peatland in China has an important effect on runoff and is of great significance for wetland ecosystem protection. However, spatio-temporal characteristics of alpine peatland surface deformation in China lack systematic studies, and the driving mechanism is not yet clear. In this study, we selected the alpine peatland of Maduo County in China as the research object, surface deformation of peatland based on the small baseline subset radar interferometry technique was obtained, we analyzed spatio-temporal deformation characteristics and patterns of peatland, explored the driving mechanism of the peatland surface deformation with single-factor and multifactor combinations of Geo-detector, respectively. The results showed that the overall subsidence rates of peatlands in Maduo County, China slowed down year by year from 2018 to 2020, but there was seasonal freezing and thawing, subsidence rates of peatlands at high elevation and high slopes were stable, peatlands at low elevation and low slope were vulnerable to disturbance, subsidence rates are largest. Maliecuo, Bailongqu, and Gaerlawangzang regions were serious subsidence, the maximum subsidence rate was 159 mm/year. Meteorological factors and geological conditions were the main reasons for the surface deformation of alpine peatland in Maduo County, China. This study provides a theoretical basis for the conservation and restoration of peatland ecosystems in the alpine regions of China.**

***Index Terms*—InSAR, peatland, remote sensing, surface deformation.**

I. Introduction

ALPINE peatlands are a special type of wetland with high altitude and low temperature [1] and are widely distributed in highland areas, such as the Qinghai-Tibet Plateau in China [2].

Manuscript received 4 December 2023; revised 17 January 2024; accepted 25 January 2024. Date of publication 29 January 2024; date of current version 13 February 2024. This work was supported in part by the National Natural Scientific Foundation of China under Grant 42201459, in part by the Young Doctoral Fund Project of Higher Education Institutions in Gansu Province under Grant 2022QB-058, in part by the State Key Laboratory of Geo-Information Engineering and Key Laboratory of Surveying and Map-ping Science and Geospatial Information Technology of MNR, CASM under Grant 2022-03-03, and in part by the Key Research and Development Project of Lanzhou Jiao tong University under Grant LZJTU-ZDYF2301. *(Corresponding author: Yi He.)*

The authors are with the Faculty of Geomatics, Lanzhou Jiaotong University, Lanzhou 730700, China and with the National-Local Joint Engineering Research Center of Technologies and Applications for National Geographic State Monitoring, Lanzhou 730700, China, and also with the Gansu Provincial Engineering Laboratory for National Geographic State Monitoring, Lanzhou 730700, China (e-mail: 2397524350@qq.com; heyi@mail.lzjtu.cn; yyangwang48@gmail.com; 119273207@qq.com).

Digital Object Identifier 10.1109/JSTARS.2024.3359712

There are 360 peat deposits in the Qinghai-Tibet alpine region of China, accounting for 18.1% of the peat deposits in China, and the peat coverage area is about 1.29×10^6 km^2, accounting for 73.7% of the total peat area in China [3]. Peatland ecosystems in alpine regions not only have ecological functions. Peatland such as water containment, biodiversity conservation, climate regulation, and carbon storage [4], but are also among the wetlands with the highest biodiversity per unit area of any ecosystem [5]. However, due to environmental changes and external disturbances, peatlands located in alpine regions are highly susceptible to shrinkage and degradation [6]. This change process leads to the gradual decomposition and oxidation of organic matter in the peat layer and the compression of the peat layer. This, in turn, causes vegetation loss and biodiversity decline in the peatlands of the region and affects carbon and nitrogen cycling and gas fluxes [7], caught in a vicious cycle of climate warming and peatland degradation. Therefore, research on peatlands in alpine regions is extremely urgent.

As part of the alpine regions of China, the peatlands of Maduo County have high carbon sequestration potential due to high soil organic matter content and low decomposition level [8]. However, due to overgrazing and climate change, the peatlands in Maduo County have been degraded to varying degrees [9]. Li et al. [10] found that all six types of peatlands in Maduo County suffered losses between 1990 and 2001, with the greatest shrinkage in alpine peatlands. In addition, increasing temperatures and permafrost degradation are also important causes of peatland shrinkage in this region. Peatlands in Maduo County are extremely sensitive to external environmental changes [11], and the fragility of their ecosystems determines the difficulty of their recovery after shrinkage. Accurate information on the spatial distribution and temporal variation of peatland surface deformation is essential in assessing the health and evolution of peatland ecosystems [12]. Therefore, effective monitoring of characteristics of peatland surface deformation in Maduo County is important for the conservation and restoration of ecological functions of peatlands in this region.

Peatland surface deformation monitoring includes both traditional methods and InSAR techniques. Traditional methods are mainly anchored in porous PVC pipes on peat substrate

[13] and differential global positioning systems [14]. Traditional methods are not applicable in terms of time, cost, and scale due to vegetation or forest barriers, making it difficult to assess large-scale peatland subsidence features [15]. InSAR technique for monitoring peatland surface deformation has some distinct advantages:

1) high relative accuracy (millimeter level);
2) high spatial resolution (meters to tens of meters);
3) wide coverage; and
4) availability of long-term archived historical data, offering the possibility to study the evolution of the historical peatland surface.

In recent years, time-series InSAR techniques have been applied to monitor peatland surface movement conditions, for example, Hrysiewicz et al. [16] used the time-series InSAR technique and Sentinel-1 C-band radar data to obtain long-term subsidence of raised peatlands at Ballynafagh, Co. Kildare, Ireland from 2017 to 2021. Umarhadi et al. [17] assessed the relationship between subsidence rates and LULC in tropical peatlands using the small baseline subset radar interferometry (SBAS-InSAR) method. Tampuu et al. [18] used the SBAS-InSAR technique and seasonal-annual search approach to reveal a consistent rate of peatland subsidence and validated the InSAR results through field surveys. Valman et al. [19] combined InSAR data, processed using the ASPIS algorithm to monitor ground motion between 2017 and 2021, with optical and LiDAR data to investigate the rate of subsidence across palsa peatlands in northern Sweden. The above study illustrates the feasibility of the InSAR method in peatland surface deformation monitoring. There are few InSAR studies on peatlands and most of the existing monitoring studies on peatland surface deformation are concentrated in tropical areas such as Southeast Asia and Indonesia. At present, there is a lack of attention to peatlands in alpine regions, especially in China. Due to the harsh climatic conditions and complex terrain in the alpine region, the surface monitoring of peatlands in this region is severely limited. Large-scale and long-time series monitoring of peatland deformation is still lacking, and the spatio-temporal evolution of peatland deformation and its driving mechanism under complex environment are still unclear. Therefore, it is necessary to carry out further research to study the deformation characteristics and deformation driving mechanism of alpine peatland, to provide data support for the evaluation of peatland health status and peatland management in the alpine region.

In this study, we selected Maduo County in the alpine region of China with widely distributed peatlands as the study area. InSAR technology and multiple statistical monitoring methods are used to quantify the temporal and spatial pattern of peatland deformation in the alpine region of China and elucidate the driving mechanism of the deformation. The main objectives are: 1) to reveal the spatio-temporal evolution characteristics and patterns of peatland surface deformation in Maduo County, alpine region of China based on InSAR technology; 2) to investigate the driving mechanism of peatland surface deformation based on climatic factors, geological conditions, and soil conditions. This will provide decision support for the restoration and protection of degraded peatland in the alpine region and is of great significance for the sustainable development of the alpine peatland ecosystem.

II. Materials and Methods

A. Study Area

Maduo County is located in the south of Qinghai Province, northwest of Guoluo Tibetan Autonomous Prefecture, in the core hinterland of Sanjiangyuan National Nature Reserve, with a total area of 25 253 km^2, which is a plateau area. The terrain slopes from northwest to southeast, with most of the elevation between 4500 and 5000 m. The topography is undulating and relatively flat, high in the northwest and low in the southeast. There are flat lands, desert lands, and swamps among the mountains, and highland meadows are widely distributed. The soils are mainly alpine meadow steppe soil, carbonate alpine meadow soil, and alpine meadow soil. The county has an alpine grassland climate, the annual average temperature is -4.1 °C, $\geq$ 10 °C the number of days is only 4.1 days, there are no four seasons in the year, winter is long and cold, summer is short and cool, and rainy. The territory is rich in water resources, with an average annual precipitation of 303.9 mm, 86% of which is concentrated in May-June, and an annual evaporation of 1264 mm, with large interannual variations. Its topography and hydrothermal conditions are suitable for peatland development. The peatland in Maduo County is widely distributed, with an area of about 6181.1 km^2, which is more concentrated in the southwest, especially in the southern areas of Lake Zhaling and Lake Eling [20]. In addition, most of the peatlands in the north are small, elongated, and located in valley bottoms and upland hollow slopes [21]. The peatland boundary in Maduo County was determined based on Zhou et al.'s [20] study combined with the visual interpretation of Google Earth images and field validation, its distribution is shown in Fig. 1.

B. Data Sources

The Sentinel-1A satellite was launched on April 3, 2014, carrying a C-band synthetic aperture radar. Due to the excellent performance of the radar, it is possible to acquire continuous images regardless of the weather, with a revisit period of 12 days [22]. Sentinel-1A satellite contains four operating modes: Strip Map (SM:80 km Width,5 m$\times$5 m Resolution) mode, Interferometric Wide (IW: 240 km Width, 5 m$\times$20 m Resolution) mode, Extra Wide mode (EW: 400 km Width), and Wave mode (WV: 20 km Width, 20 m$\times$5 m Resolution) [23]. Among them, the IW mode captures three subregions using a progressive topographic scan pattern, producing higher quality images that facilitate InSAR interference. In addition, the same polarization (VV) is more sensitive to the dielectric constant and surface roughness of the ground than cross-polarization [24].

In this study, 90 scenes Sentinel-1A images covering the research area from 2018 to 2021 were selected for the experiment. The date information of 90 scenes Sentinel-1A descending SAR images is shown in Table I. The images were captured through VV polarization and IW imaging mode [25]. 30 m resolution SRTM DEM from the USGS is selected. Generic atmospheric

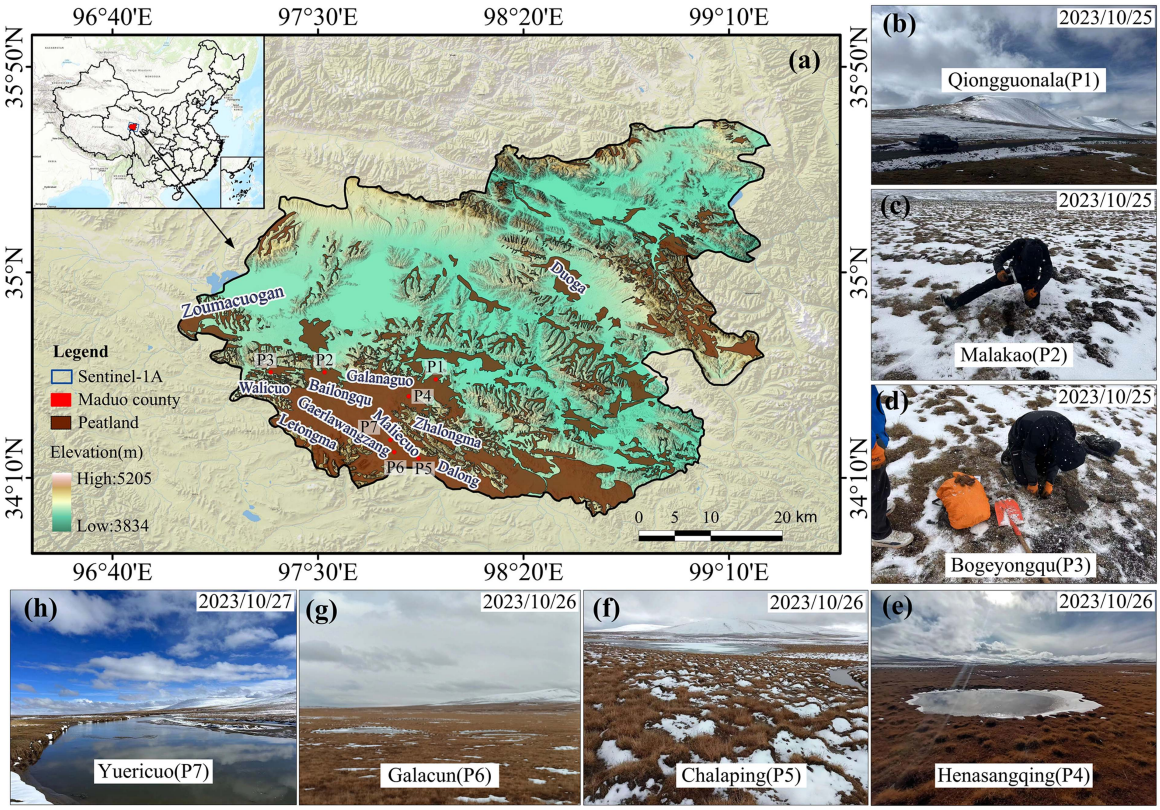

Fig. 1. (a) Location and peatland distribution in Maduo County, China. P1-P7 are field validation points. (b) Qiongguonala(P1). (c) Malakao(P2). (d) Bogeyongguo(P3). (e) Henasangqing(P4). (f) Chalaping(P5). (g) Galacun(P6). (h) Yuericuo(P7).

correction online service (GACOS) for atmospheric correction [26]. Fraction of vegetation coverage (FVC) provided by the United States geological survey. Grass-livestock balance index datasets are provided by the National Tibetan Plateau Data Center [27], which is calculated by [(actual carrying capacity-reasonable carrying capacity) $\times 100\%$] reasonable carrying capacity. Meteorological data (temperature and precipitation) are provided by the National Earth System Scientific Data and Shared Services Platform - Loess Plateau Scientific Data Center [28]. Landform-type and soil-type data from the International Soil Reference and Information Center [29]. Underground soil moisture data are from the National Tibetan Plateau Data Center [30]. To unify the spatial resolution size, all data were standardized to match the spatial resolution of the projection coordinate system WGS 84 and the Sentinel-1A mapping resolution of 1 km. The specific information is shown in Table II.

C. Methodology

In this study, we obtain the surface deformation information of peatlands in Maduo County based on the SBAS-InSAR technique and analyze the time series deformation pattern of peatlands. We quantify the driving mechanism of peatland deformation information based on climatic factors, geological conditions, and soil moisture using Geo-detector. The main technical process is shown in Fig. 2.

1) SBAS-InSAR Algorithm: SBAS-InSAR technology was first proposed by Berardino [31] in 2002. It is one of the methods of time series interferometry, which uses the multitime series InSAR technology to reduce spatial incoherence. Singular value decomposition is used to solve for deformation rates, isolated SAR data sets in larger spatial baselines can be connected to improve the temporal sampling rate of the observed data [32]. The high-density spatiotemporal information of SBAS-InSAR can effectively eliminate the influence of atmospheric effects and make the measurement results more accurate [33].

The specific principle of SBAS-InSAR is as follows.

M scenes SAR images covering the study area are acquired from t_1 to t_m period time, and then one of them is selected as the master image, and *M* sets of short baselines composed of images are obtained by the short baseline technique, and then *N* interferograms are generated according to the principle of interferometric combination and satisfy the following relations [33]:

$$\frac{M}{2} \leq N \leq \frac{M(M-1)}{2}. \tag{1}$$

Taking the moment t as the reference fiducial time, for the ith differential interferogram generated from the images at two times t_A and t_B, the interference phase corresponding to any one-pixel point (x, r) can be expressed as

$$\Delta\varphi_i(x,r) = \varphi_{\mathrm{A}}(x,r) - \varphi_{\mathrm{B}}(x,r) \approx \Delta\varphi^i_{\mathrm{def}}(x,r) + \Delta\varphi^i_{\varepsilon}(x,r) + \Delta\varphi^i_{\alpha}(x,r) + \Delta\varphi^i_{\mathrm{noi}}(x,r) \tag{2}$$

TABLE I
DATA INFORMATION OF 90 SCENES DESCENDING SENTINEL-1A SATELLITE SAR IMAGE

Image number	Image data	Image number	Image data	Image number	Image data
0	2018/01/12	31	2019/02/12	62	2020/02/19
1	2018/01/24	32	2019/02/24	63	2020/03/02
2	2018/02/05	33	2019/03/08	64	2020/03/14
3	2018/02/17	34	2019/03/20	65	2020/03/26
4	2018/03/01	35	2019/04/01	66	2020/04/07
5	2018/03/13	36	2019/04/13	67	2020/04/19
6	2018/03/25	37	2019/04/25	68	2020/05/01
7	2018/04/06	38	2019/05/07	69	2020/05/13
8	2018/04/18	39	2019/05/19	70	2020/05/25
9	2018/04/30	40	2019/05/31	71	2020/06/06
10	2018/05/12	41	2019/06/12	72	2020/06/18
11	2018/05/24	42	2019/06/24	73	2020/06/30
12	2018/06/05	43	2019/07/06	74	2020/07/12
13	2018/06/17	44	2019/07/18	75	2020/07/24
14	2018/06/29	45	2019/07/30	76	2020/08/05
15	2018/07/11	46	2019/08/11	77	2020/08/17
16	2018/07/23	47	2019/08/23	78	2020/08/29
17	2018/08/04	48	2019/09/04	79	2020/09/10
18	2018/08/16	49	2019/09/16	80	2020/09/22
19	2018/09/21	50	2019/09/28	81	2020/10/04
20	2018/10/03	51	2019/10/10	82	2020/10/16
21	2018/10/15	52	2019/10/22	83	2020/10/28
22	2018/10/27	53	2019/11/03	84	2020/11/09
23	2018/11/08	54	2019/11/15	85	2020/11/21
24	2018/11/20	55	2019/11/27	86	2020/12/03
25	2018/12/02	56	2019/12/09	87	2020/12/15
26	2018/12/14	57	2019/12/21	88	2020/12/27
27	2018/12/26	58	2020/01/02	89	2021/01/08
28	2019/01/07	59	2020/01/14	90	2021/01/20
29	2019/01/19	60	2020/01/26		
30	2019/01/31	61	2020/02/07		

where t_A and t_B ($t_A > t_B$) are the SAR image acquisition times corresponding to the ith interferogram; $\Delta\varphi^i_{\text{def}}(x,r)$ is the deformation corresponding to the range of t_A and t_B slopes; $\Delta\varphi^i_{\varepsilon}(x,r)$ is the topographic phase error; $\Delta\varphi^l_{\alpha}(x,r)$ is the atmospheric phase error; $\Delta\varphi^i_{\text{noi}}(x,r)$ is the noise phase error.

Assuming that the deformation rates between different interferograms are $v_{i,\ i\text{-}1}$, the cumulative deformation variables from t_B to t_A can be expressed as follows:

$$\Delta\varphi^i_{\text{def}}(x,r) = \frac{4\pi}{\lambda} \sum_{k=t_{\text{B}},i+1}^{t_{\text{A}},i} (t_k - t_{k-1})\, v_{k,k-1}. \quad (3)$$

Three-dimensional phase unwrapping of N-view SAR image interferograms can be used to calculate the deformation rate of SAR images at different acquisition times.

In this study, 90 views of Sentinel-1A SLC images covering the study area from January 2018 to January 2021 are selected. The experimental platform is ENVI 5.6 and SARscape5.6.2. The specific process is as follows.

The first step is to combine interference pairs and generate connection diagrams (as shown in Fig. 3). The acquired data are grouped and paired by temporal and spatial thresholds. The image of July 30, 2019, is automatically selected as the master image for this study. Due to the short-time interval of the selected image acquisition, the maximum time baseline threshold is set to 60 days and the maximum spatial threshold is set to 5%.

The second step is the interferometric workflow processing, which includes registration, interference, de-leveling effect, filtering, and phase unwrapping. The master image is the reference image throughout the processing, and all processed slant pairs

TABLE II
DETAIL INFORMATION OF DATA

Data name	Period	Data resource	Type (Resolution)	Purpose
Sentinel-1A	2018-2021	https://search.asf.alaska.edu/	Raster (5m×20m)	Monitoring peatland surface deformation
SRTM DEM	2003	https://earthexplorer.usgs.gov/	Raster (30 m×30m)	Removal of topographic phases, geocoding
GACOS	2018-2021	http://www.gacos.net/	Raster (90m×90m)	Correction of InSAR measurements
FVC	2021	http://lpdaac.usgs.gov/	Raster (250m×250m)	Explore the cause of greater peatland subsidence
Grass-Livestock Balance Index	2019	https://doi.org/10.11888/Ecolo.tpdc.271512.	Raster (1km×1km)	
Temperature	2018-2021	http://www.geodata.cn/index.html	Raster (1km×1km)	
Precipitation	2018-2021	http://www.geodata.cn/index.html	Raster (1km×1km)	Peatland surface deformation driven analysis
Landform	2019	https://www.isric.org	Vector	
Soil type	2019	https://www.isric.org	Vector	
Soil moisture	2019	https://data.tpdc.ac.cn	Raster (1km×1km)	

are aligned on this reference geometry. The multilook number is set to 4:1 in the range direction and azimuth direction of the aligned image. Atmospheric correction is performed using the GACOS and the height-dependent atmospheric phase distortion filter during interferometric and interferometric superposition processing, calculating coherence and performing complex conjugate multiplication to obtain interferograms. The generated interferogram contains the topographic phase, atmospheric phase, deformation phase, orbital phase, and noise phase. The SRTM-DEM is used to remove the topographic phase [34], and the Goldstein adaptive filtering algorithm is used to filter the interference phase to remove the noise phase. Since peatlands in the study area contain some water bodies and vegetation, the coherence threshold is adjusted to 0.25 to avoid serious decoherence. The phase points with coherence greater than 0.25 are formed into a Delaunay triangular network, and the minimum cost flow algorithm is applied for phase unwrapping. The interferograms with good quality are selected, the connection pairs are edited, and the remaining 164 interferometric pairs are involved in the subsequent inversion.

The third step is the first inversion. The GCP points with good coherence and far from the deformation region are automatically selected for estimating and removing the residual constant phase and the phase ramp that still exists after unwrapping. The first estimate of deformation rate and residual topography.

The fourth step is the second inversion. The atmospheric phase is removed by temporal highpass filtering and spatial lowpass filtering to obtain a purer final displacement result on the time series.

The fifth step is geocoding. DEM is used as a reference to convert the SAR coordinates into geographical coordinates to obtain the subsidence rate as well as the time-series cumulative subsidence in the study area.

2) PS-InSAR Algorithm: PS-InSAR method was proposed by Ferretti [35], this technique is based on the magnitude and phase information of the image to detect highly correlated and stable points, i.e., permanent scatterers [36]. In this study, the results of PS-InSAR technology are cross-verified with SBAS-InSAR.

A total of 22 views of Sentinel-1A images in 2018 are selected as validation data to monitor the surface deformation of peatlands in Maduo County using the PS-InSAR method under the SARscape module of the ENVI platform. The image on May 24, 2018, is automatically selected as the reference image, and the other slave images are registered with the reference image, and the coordinate system is consistent with the reference image. Interferometric phase deleveling is performed using SRTM DEM (30 m resolution), filtering uses the Goldstein method, deleveling and calculation of orbital phase use the polynomial fitting method, estimation of residual topography and deformation rates uses linear models, geocoding is performed with a coherence factor of 0.7.

3) Geo-Detector Method: Geo-detector is a statistical method proposed by Wang and Xu [37], which can detect spatial anisotropy as well as reveal the driving forces. If the independent variable has a spatially significant effect on the occurrence of the dependent variable, then the spatial distribution of the independent variable should be similar to that of the dependent variable. This method can not only detect the influence of a single factor but also determine the strength, direction, and linearity of multifactor interactions. In this study, we mainly used factor detectors, interaction detectors, and ecological detectors to detect the driving mechanisms of different impact factors (X) on the surface deformation (Y) of peatlands in Maduo County.

Factor detection detects the extent to which factor X explains the spatial variability of Y, expressed as a q value. Larger values of q indicate more pronounced spatial heterogeneity of Y. If the stratification is generated by the independent variable X, a larger value of q indicates a stronger explanatory power of the independent variable X for attribute Y, and vice versa. Interaction detection identifies interactions between different risk factors X_S and assesses whether factors X_1 and X_2 together increase or decrease the explanatory power of the dependent variable Y. Ecological detectors are used to compare whether there is a

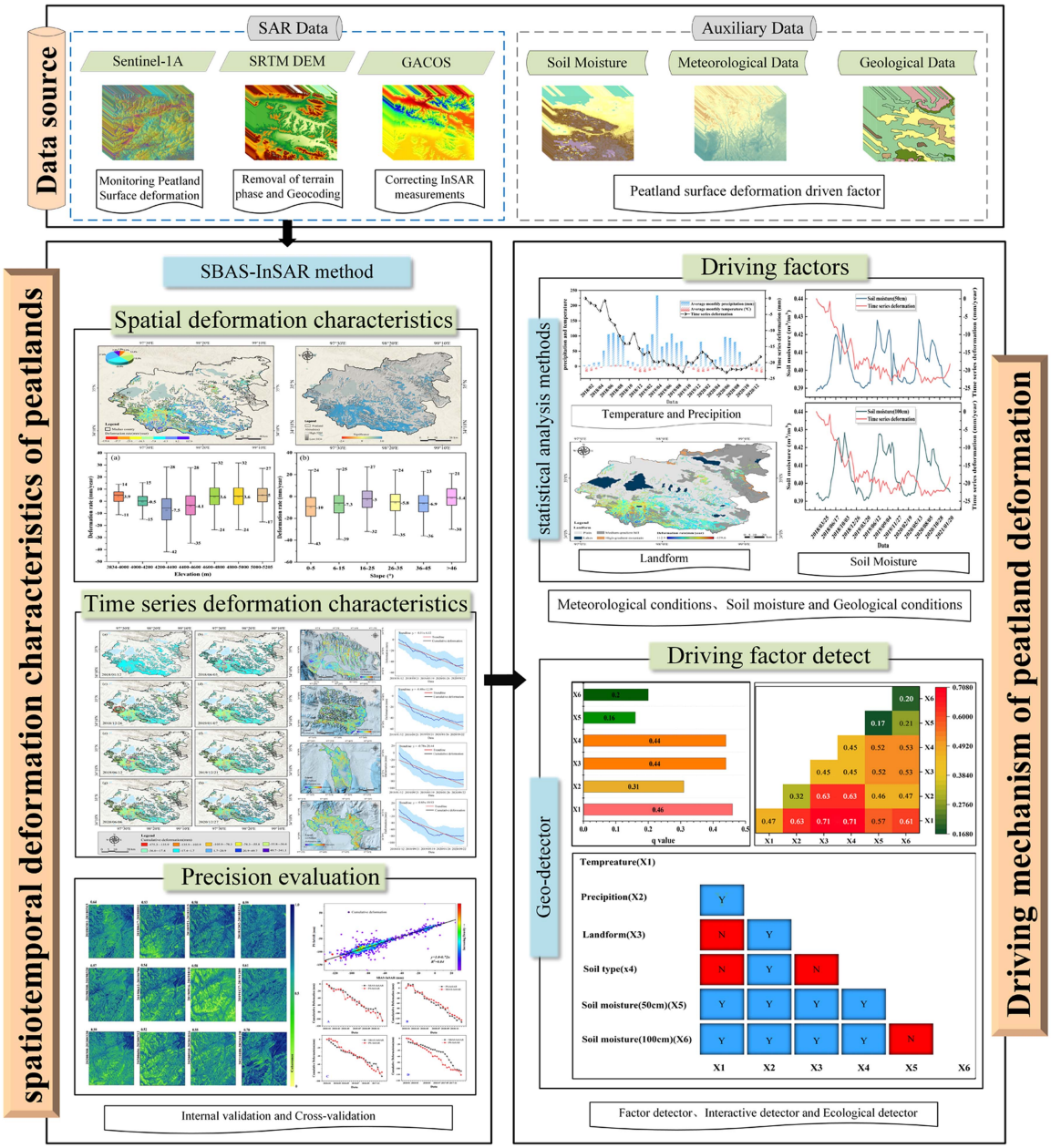

Fig. 2. Flow chart of this study.

significant difference in the effect of the two factors X_1 and X_2 on the spatial distribution of attribute Y [37].

In this study, the study area was gridded at 1 km × 1 km using the Fishnet tool in ArcGIS 10.8. Vector points are generated at the geometric center of the grid, and the average deformation rate data, meteorological data (temperature and precipitation), geological data (landform type data), and soil conditions (soil type and soil moisture) are extracted from the study area and stratified using the natural breakpoint method. The meteorological data, geological data, and soil moisture data are used as X data of the geo-detector, and Y data represent the average deformation rate data. X and Y data are input into Geo-detector for factor detection, interaction detection, and ecological detection.

III Results and Analysis

A. Spatial Characteristics of Peatland Surface Deformation

The average peatland surface deformation rate in the study area was obtained based on Sentinel-1A images using SBAS-InSAR (see Fig. 4), with negative values representing subsidence and positive values representing uplift. It was found that 53.5% of peatlands had a surface deformation rate of -7.8 to 9.2 mm/year, and peatlands were relatively stable. However, 39.2% of peatlands in Maduo County showed surface subsidence, which mainly concentrated in Zoumacougan (S1), Walicuo (S2), Letongma (S3), Galanaguo (S4), Bailongqu (S5), Gaerlawangzang (S6), Maliecuo (S7), Dalong (S8) and Duoqu (S9) and other regions. Among them, the surface subsidence rate

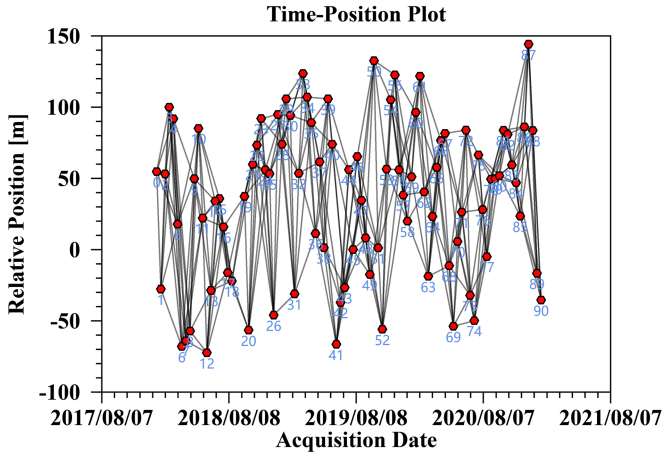

Fig. 3. SBAS-InSAR spatiotemporal baseline map.

of Bailongqu peatland was the largest. The InSAR results were verified by field investigation along national Highway G0613 in Henaqu(V1), Galaqu(V2) and Yueyi(V3). We found that the uneven degradation of the peatland in the study area is serious, which is the main reason for the subsidence of the peatland.

There are two inter-related types of peatland surface deformation, the first is surface subsidence due to oxidation in the peat layer above water table, and the second is shrinkage and expansion due to oscillated groundwater levels (GLs). The identified peatland surface deformation data from Sentinel images should be the combination of both, which is why in some peatland areas, the peatland values are positive (see Fig. 4).

Consider that peatland subsidence releases large amounts of carbon dioxide, wreaking havoc on ecosystems. This study focuses on peatland subsidence. We screened the subsidence points (peatland deformation less than 0) of each deformation result from 2018 to 2021, and used the Mann-Kendall test to draw the subsidence significance change curve to analyze the changing trend of peatland subsidence in Maduo County (see Fig. 5), with positive values (significance value greater than 0) representing significant subsidence and negative values (significance value less than 0) representing insignificant subsidence. From Fig. 5, most of the subsidence areas of peatland in Maduo County have significant subsidence, and only a few subsidence points have no significant subsidence.

To explore the reasons for the large subsidence areas of peatland surface subsidence rates exceeding 16.3 mm/year (see Fig. 4). In this study, galanaguo, bailongqu, gaerlawangzang and liemucuoka regions with subsidence value and wide distribution of subsidence area were selected to compare the value of peatland surface deformation rates and Grass-livestock Balance Index. At the same time, we verified the degradation signs of peatland on Google Earth image and identified the degradation range of peatland (dark brown area in Google Earth image), the results are shown in Fig. 6. The distribution area of the large peatland subsidence, FVC, the Grass-Livestock Balance Index and the degradation range of peatland are essentially consistent. In the degraded area of peatland, the surface subsidence value is larger and the grass-livestock balance index is smaller, which indicates that the greater subsidence of peatland is caused by peatland degradation. This process is due to the increase of biomass and grazing activities, which leads to the degradation of alpine meadows, the imbalance of grass storage, the oxidation of peatland, and the release of a large amount of CO_2, subsequently, surface subsidence occurs in the peatland.

Topography plays an important role in controlling the evolution of peatlands [20]. In this study, one-way ANOVA in hypothesis testing was used to test whether there were differences in the distribution of surface deformation rates in peatlands at different elevations and slopes, the results were shown in Tables III and IV. In Tables III and IV, the intergroup significance values of peatland surface deformation rates at different elevations and slopes are all less than 0.001, indicating that there are significant differences in the distribution of peatland surface deformation rates at elevations and slopes among all groups, as well as peatlands distributed on different topographies differ in their development and surface deformation patterns.

The distribution of surface deformation rates of peatlands at different elevations and slopes in the study area was calculated (see Fig. 7). Overall, the mean deformation rates of peatlands at different elevations in the study area varied greatly [see Fig. 7(a)]. Peatland subsidence rates at high elevations (above 4600 m) are lower than those at middle elevations (4200–4600 m) and low elevations (below 4200 m), with a maximum difference of 31 mm/year, and the median of peatland subsidence rates at high elevations is smaller. This indicates that peatlands at high elevations are less susceptible to environmental impacts and more stable, while peatlands at middle and low elevations are more susceptible to environmental infestation. Peatlands at lower elevations may be particularly susceptible to changes because hydrological cycles that control water tables are likely to vary the most [39]. The sustainability of mountain peatlands occurring at the middle and lower end of the known elevation range may be particularly susceptible to a changing climate, as these peatlands already experience lower snowpack, earlier snow melt, and warmer growing season air temperatures [39]. In high-elevation peatlands, slow decomposition rates result from a nutrient-poor substrate resistant to decay [40]. Due to greater snowpack and the later onset of melt, the high-elevation sites had the lowest air temperatures and highest water tables [39].

We reference to Olorunfemi et al.'s [41] grading criteria for slope differentiation, the slopes were categorized into six classes based on the topographic conditions of the study area [see Fig. 7(b)]. 0°–5° is a flat slope, 5°–15° is a gentle slope, 15°–25° is a ramp, 25°–35° is a steep slope, 35°–45° is a sharp slope, and >45° is a dangerous slope. Overall, the average deformation rate of peatland with different slopes in the study area is different. From the flat slope to the ramp, the maximum subsidence rate and the extreme difference both showed a decreasing trend, and the median was less than 0, indicating that the subsidence was gradually slowing down. The present concave morphology of the peat surface in the gentle slope probably results from compaction and oxidation in response to regionally lowered GLs [42]. From ramp to sharp slopes, the maximum and median subsidence rates gradually increased and peatland subsidence intensified. The peatlands on steep and sharp slopes had a similar distribution

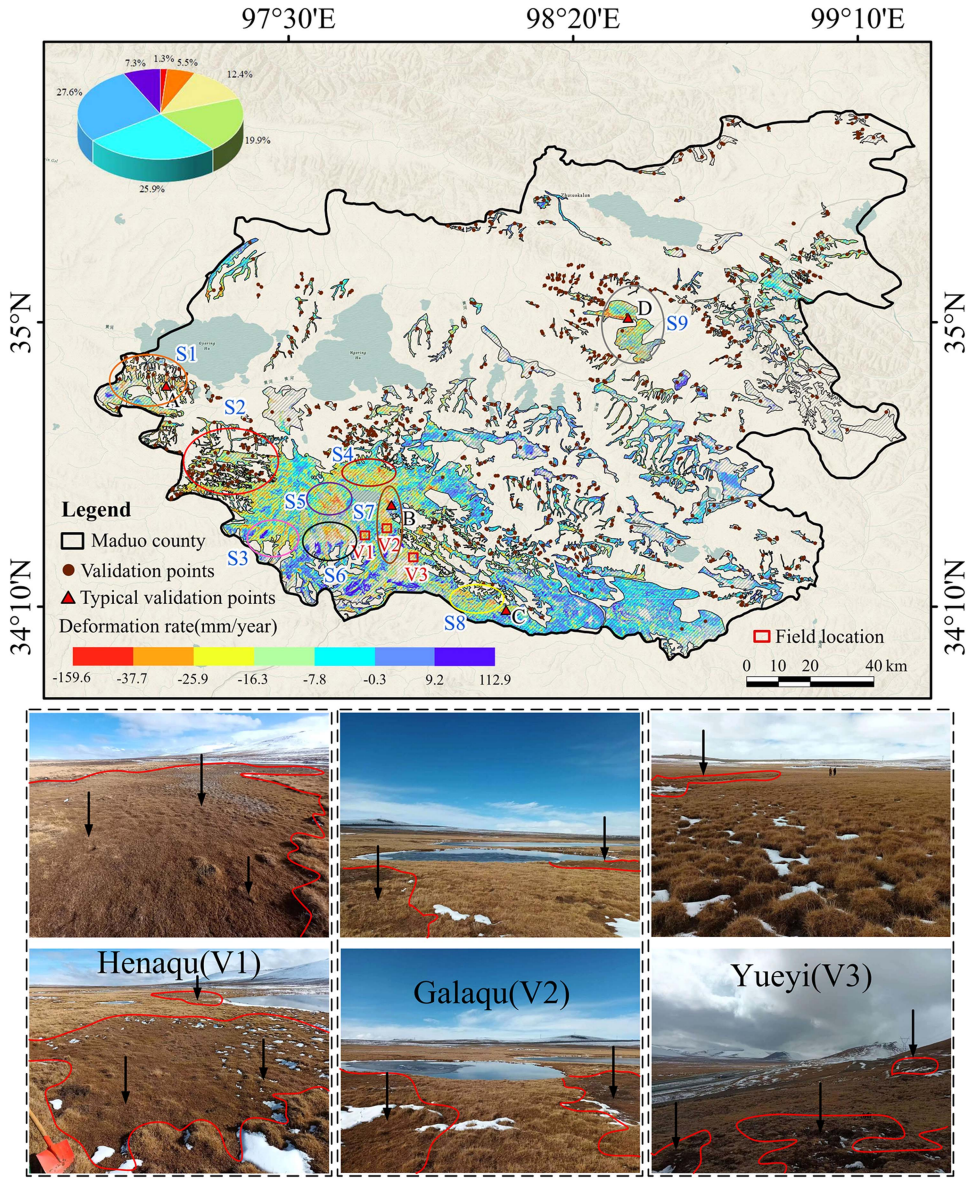

Fig. 4. Average vertical deformation rate of peatlands in Maduo County from January 12, 2018 to January 20, 2021, the mapping resolution is 15×15 meters. V1–V3 are field validation areas. V1(henaqu). V2(Galaqu). V3(Yueyi). S1–S9 are typical peatland deformation areas. A, B, C and D are typical validation point.

TABLE III
SIGNIFICANCE TEST FOR THE DIFFERENCE IN THE DISTRIBUTION OF MEAN PEATLAND SURFACE DEFORMATION RATE AT DIFFERENT ELEVATIONS

mean peatland deformation rate		Sum of squares	Degrees of Freedom	Mean Square	F	Statistical significance
Between-Group(combination)		7365358.3	6	1227559.7	10195.2	<0.001
Liner term	unweighted	64736.5	1	64736.5	537.6	<0.001
	weighted	3357202.2	1	3357202.2	27882.3	<0.001
	bias	4008156.2	5	801631.2	6657.7	<0.001
within-group		41028182.9	30749	120.4		
total		48353941.3	30755			

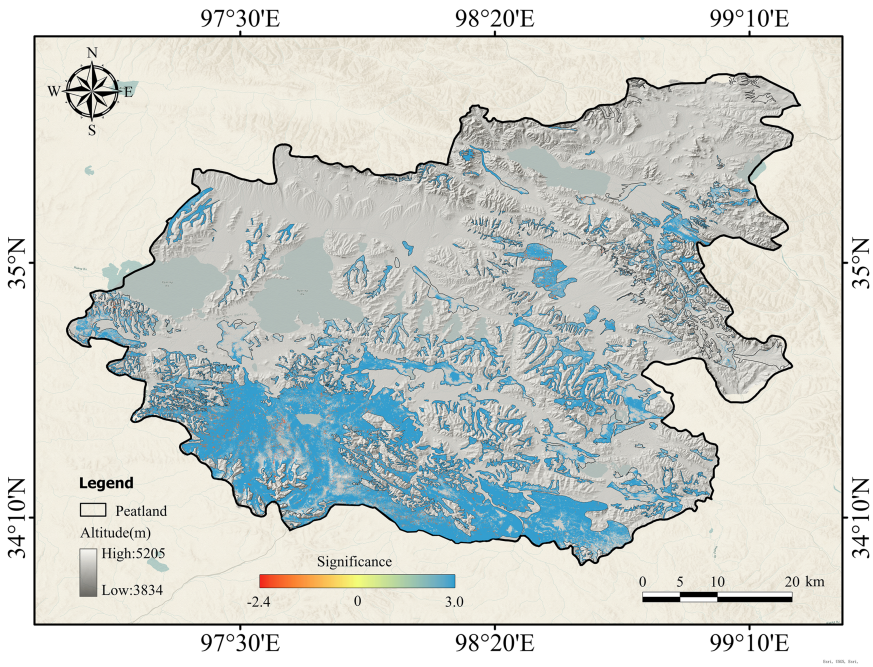

Fig. 5. Significant subsidence test of peatland.

TABLE IV
SIGNIFICANCE TEST FOR THE DIFFERENCE IN THE DISTRIBUTION OF MEAN PEATLAND SURFACE DEFORMATION RATE AT DIFFERENT SLOPES

mean peatland deformation rate		Sum of squares	Degrees of Freedom	Mean Square	F	Statistical significance
Between-Group(combination)		14749622.8	5	2989524.6	18515.1	<0.001
Liner term	unweighted	28325.9	1	28325.9	175,4	<0.001
	weighted	11822160.3	1	3357202.2	73218.4	<0.001
	bias	3125462.5	4	11822160.3	4839.2	<0.001
within-group		419186135.6	2596153	161.5		
total		434133758.4	2596158			

of deformation rates. Due to steep gradients and rapid surface runoff, this steep slope is unlikely to be conducive to the water ponding that is necessary to maintain high water tables for peatland development [43], the development of peatland is affected by hydrologic regulation. The peatlands on the dangerous slopes were less distributed, the rate of peatland deformation was smaller, and the peatland development was stable. Likely because the upper slope section serves as a catchment area that increases water supply to these areas [43], and the thicker and impermeable permafrost layer further minimizes water loss [44], peatland development is relatively stable. From the perspective of elevation and slope, the peatland with high elevation and high slope is stable, while the peatland with low elevation and low slope is susceptible to disturbances.

The aspect is divided into eight directions at an interval of 45°. 0°–22.5° and 337.5°–360° together form the east, 22.5°–67.5° is the northeast, and so on. The south, southeast, and southwest slopes are collectively called the sunny aspect, and the north, northwest, and northeast aspects are collectively called the shady aspect. Fig. 8 shows the distribution of deformation rate image elements with different aspects upward. As can be seen from Fig. 8, the percentage of deformation image elements on the shady aspect is higher than that on the sunny aspect, with the highest percentage of 17% on the shady aspect and the lowest percentage of 10% on the sunny aspect. The sunny aspect has sufficient sunshine, better water and heat conditions, and lush vegetation. The monitored peatlands had more incoherent images of deformation. However, the deformation image elements were evenly distributed in the proportion of each aspect, and the overall variability was small.

B. *Time-Series Deformation Characteristics of Peatlands*

The annual average peatland surface deformation rates from 2018 to 2020 in Maduo County were calculated by the time-weighted method, and the natural breakpoint method was used to categorize the annual average peatland surface deformation rates into 10 categories (see Fig. 9). The maximum peatland surface

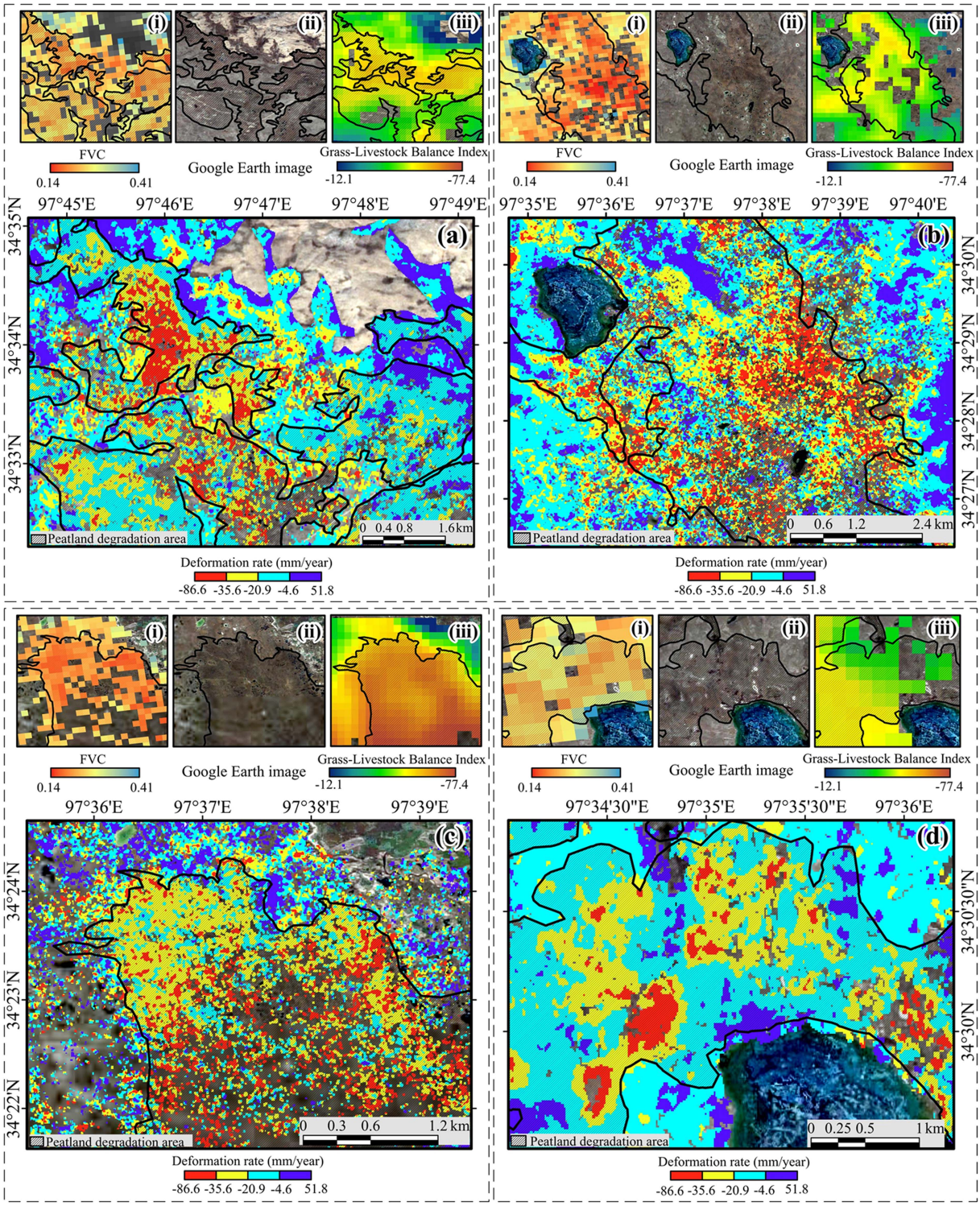

Fig. 6. Surface deformation in heavily peatland degraded areas. (a) Galanaguo part area. (b) Bailongqu part area. (c) Gaerlawangzang part area. (d) Liemucuoka part area. The base map is Google Earth image. (i), (ii) and (iii) FVC, degradation extent, and grass-livestock balance Index of four peatland degradation areas (a), (b), (c) and (d), respectively.

deformation rates from 2018 to 2020 were -217.9 mm/year, -172.8 mm/year, and -158.4 mm/year, respectively. Compared to 2018, there were significantly fewer areas with subsidence rates exceeding 52.2 mm/year in 2019 and 2020, and the spatial distribution of peatland subsidence areas was also relatively decreased. Three typical regions (a1, a2, and a3) with high deformation rates were selected to compare the time series characteristics of peatland deformation rates from 2018 to 2020. From the magnified view of the three typical regions, it could be more clearly observed that the peatland deformation rates and

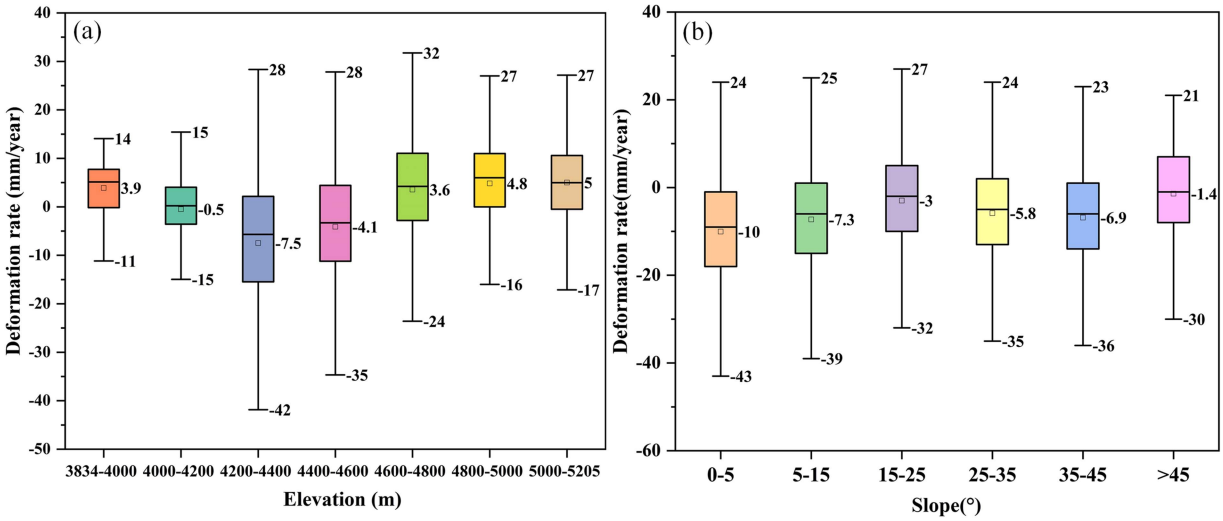

Fig. 7. Distribution of the average deformation rate of peatland surface at different elevations and slopes. (a) Elevation. (b) Slope.

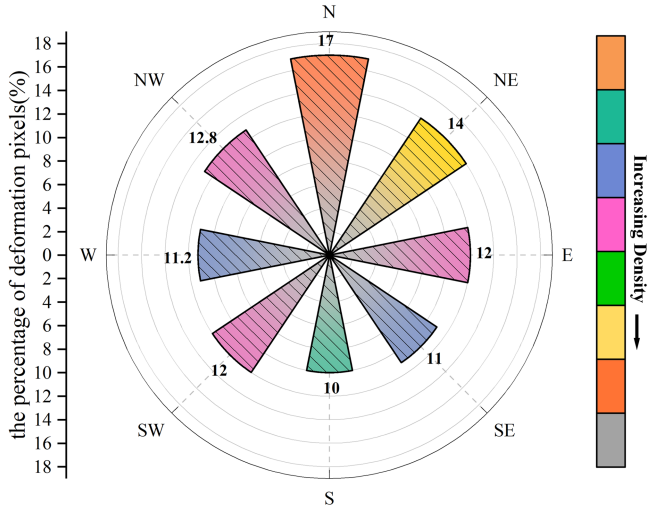

Fig. 8. Average deformation rate image element percentage for different aspects.

deformation areas in the three regions in 2019 and 2020 were significantly less than in 2018, which was consistent with the overall deformation trend. The study found that most peatland subsidence slowing down year by year and the trend of peatland degradation has been mitigated.

To reveal in detail the time series evolution characteristics of peatland deformation in Maduo County from 2018 to 2021, time series deformation maps with a time interval of about 6 months were selected to plot the time series of cumulative deformation in the vertical direction in the region. The natural breakpoint method was used to categorize the time series peatland cumulative deformation into 10 categories (see Fig. 10). From January to June 2018, peatland deformation increased over time in the main deformation areas of Letongma (S3), Galanaguo (S4), Bailongqu (S5), and Gaerlawangzang (S6) in Maduo County. In December 2018, peatland surface deformation increased in the regions of Zoumacuogan (S1), Walicuo (S2), Dalong (S8), and Duoqu (S9). In June 2019, the extent of peatland deformation and deformation variables in Maduo County increased rapidly, especially in Maliecuo, Bailongqu, and Gaerlawangzang, and the increasing trend continued until January 2021.

To further investigate the time series evolutionary characteristics of peatland surface deformation in Maduo County, we counted the mean cumulative deformation values of Zoumacuogan, Walicuo, Bailongqu, and Galanaguo, where the high coherence and significant deformation, calculated the time series trend curve of peatland surface deformation [45] (see Fig. 11). The subsidence trend was basically the same at the four regions. A significant increase in the deformation rate from January 2018 to September 2018, with a maximum cumulative deformation of -44.1 mm. The rate of deformation slowed from September 2018 to February 2019, with a maximum cumulative deformation of -59.9 mm. From February 2019 to September 2019, a clear trend of subsidence was evident, but a slight uplift occurred until March of the following year. Subsidence increased again from March 2020 to September 2020, and this trend slowed down again after September of the same year. The above analysis revealed that the surface deformation of peatlands in Maduo County showed seasonal freezing, swelling, and thawing.

IV. Discussion

A. Evaluation of Peatland InSAR Deformation Accuracy

To ensure the accuracy of the time-series InSAR deformation results of the peatlands in Maduo County, the internal validation of the time-series deformation results of the peatlands was performed based on the mean coherence coefficient stability point [46]. Coherence maps of different periods with close time intervals are selected from the filtered temporal interference pairs for comparison. As shown in Fig. 12, the darker the green area, the larger the value of the coherence coefficient, the better the coherence, and the more reliable the interference phase results.

The time interval was similar as seen in the time-series coherence plot, and the coherence and average coherence coefficients differed significantly from season to season. The correlation

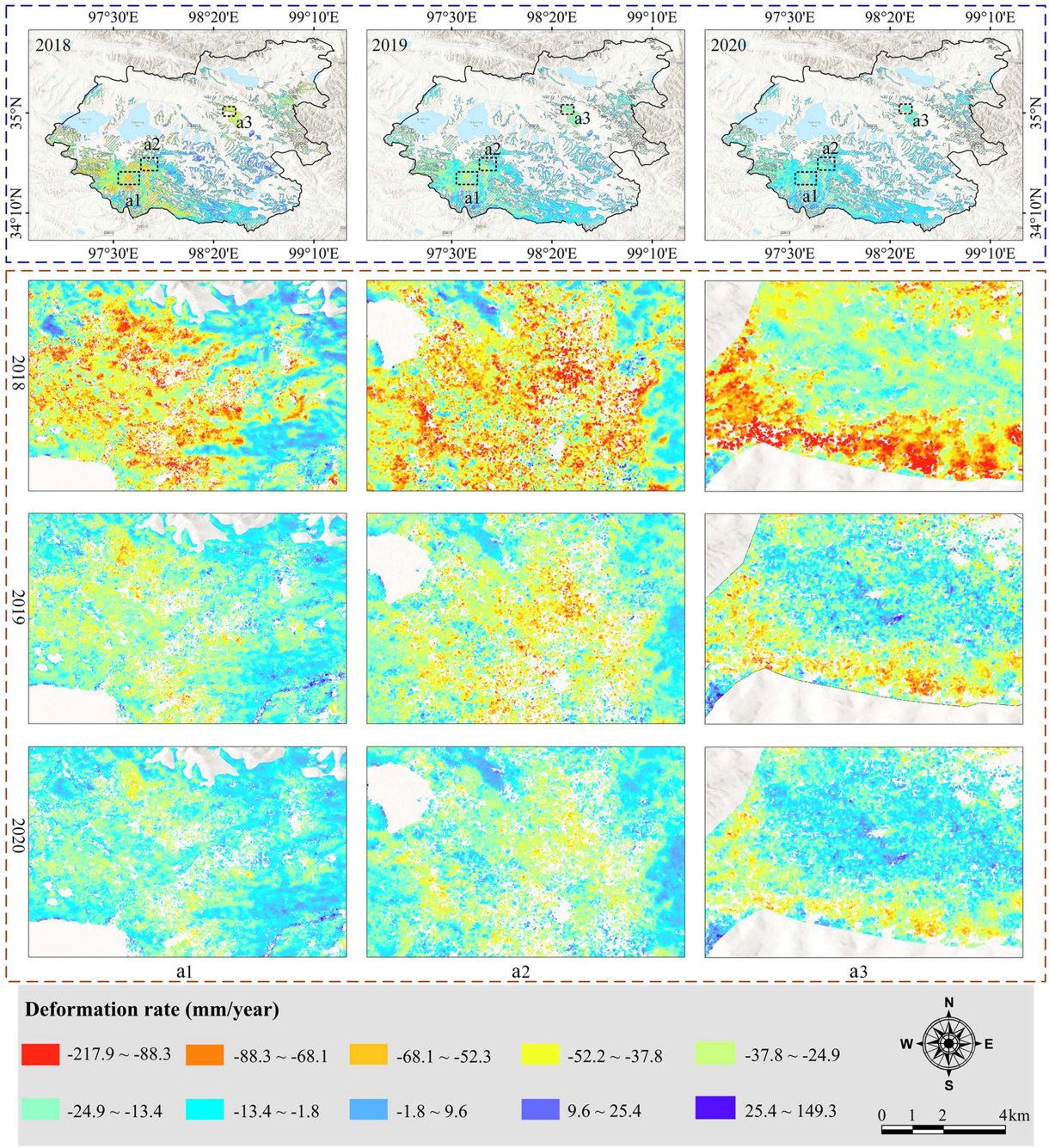

Fig. 9. Interannual variation of peatland surface deformation rate in Maduo County.

coefficient values were, in descending order, Winter > Spring > Fall > Summer. Seasonal changes in coherence were thought to be the result of changes in vegetation cover [47]. Although the average coherence coefficient values were low in summer, the average coherence coefficient values of the screened time-series interference pairs in the study area were maintained above 0.5, ensuring the accuracy of peatland SBAS-InSAR results [48]. To further verify the peatland SBAS-InSAR results, a total of 28 views Sentinel-1A images in 2018 were selected and cross-validated using PS-InSAR results [49]. The monitoring results of two time-series analysis methods (PS-InSAR and SBAS-InSAR) were correlated by randomly selecting 800 points in the validation area (the distribution of random validation points is shown in Fig. 4). As shown in Fig. 13, the correlation between the two monitoring results was high, with $R^2 = 0.84$, indicating that the monitoring results were reliable. Most of the points in Fig. 13 were concentrated, and the cumulative deformation variables are mainly distributed between -60 and -110 mm, and a few points are discrete. There are also very few outliers, which is due to the different implementations of the two methods, PS-InSAR technology is more suitable for monitoring surface deformation changes in urban areas with abundant surface objects than SBAS-InSAR technology [49].

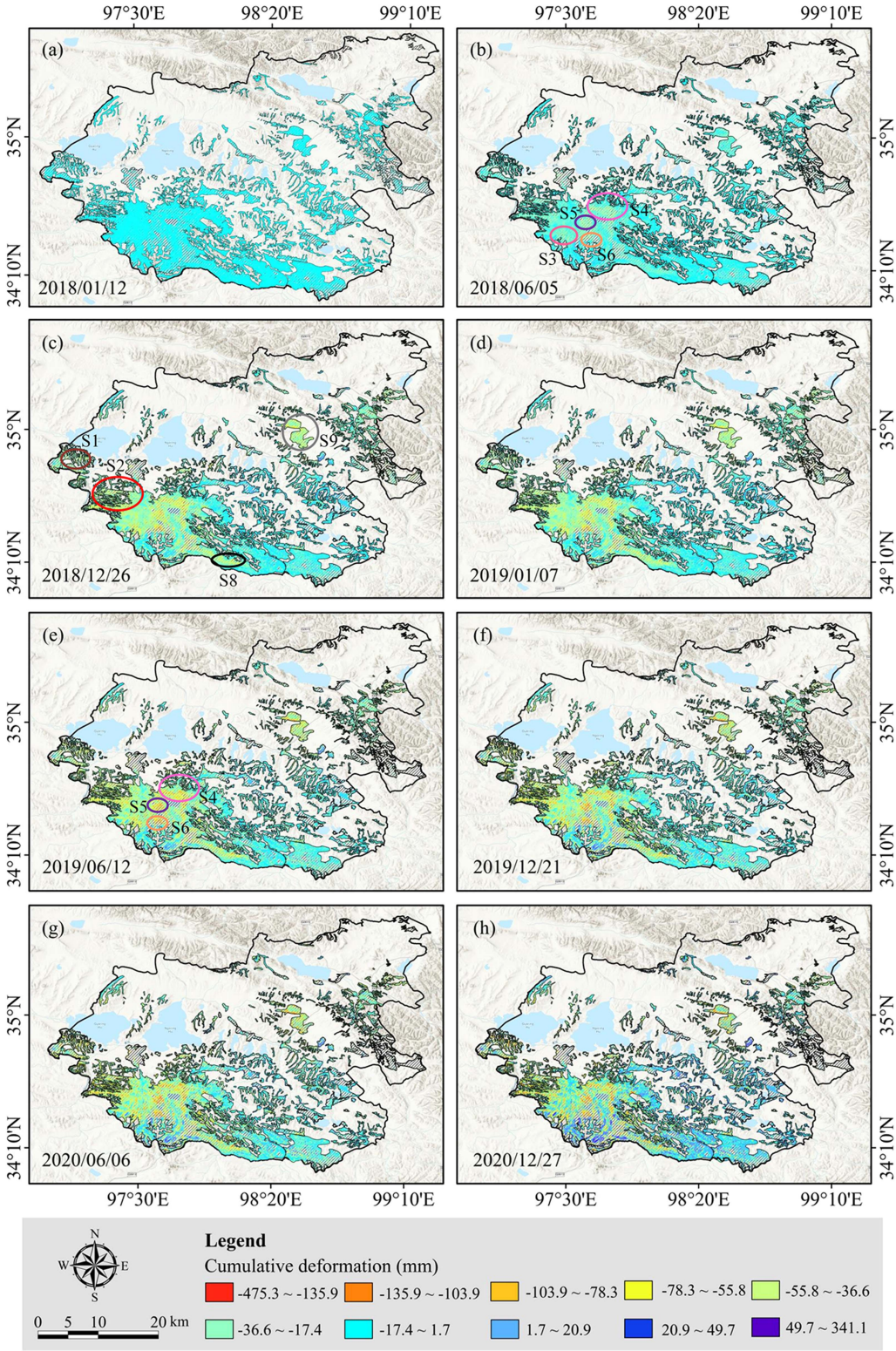

Fig. 10. Time series peatland cumulative deformation variables.

Four deformation points with high coherence and large deformation were further selected to compare the temporal monitoring results of PS-InSAR and SBAS-InSAR (typical validation points A, B, C, and D are shown in Fig. 4). The temporal deformation trends monitored by the two methods at points A, B, C, and D shown in Fig. 13 were generally consistent. Time-series deformation values monitored by the PS-InSAR method at points A, B, C, and D are greater than those monitored by the SBAS-InSAR method, and the differences were -2.35, -7.88, -10.82, and -12.88 mm. The cross-validation of the

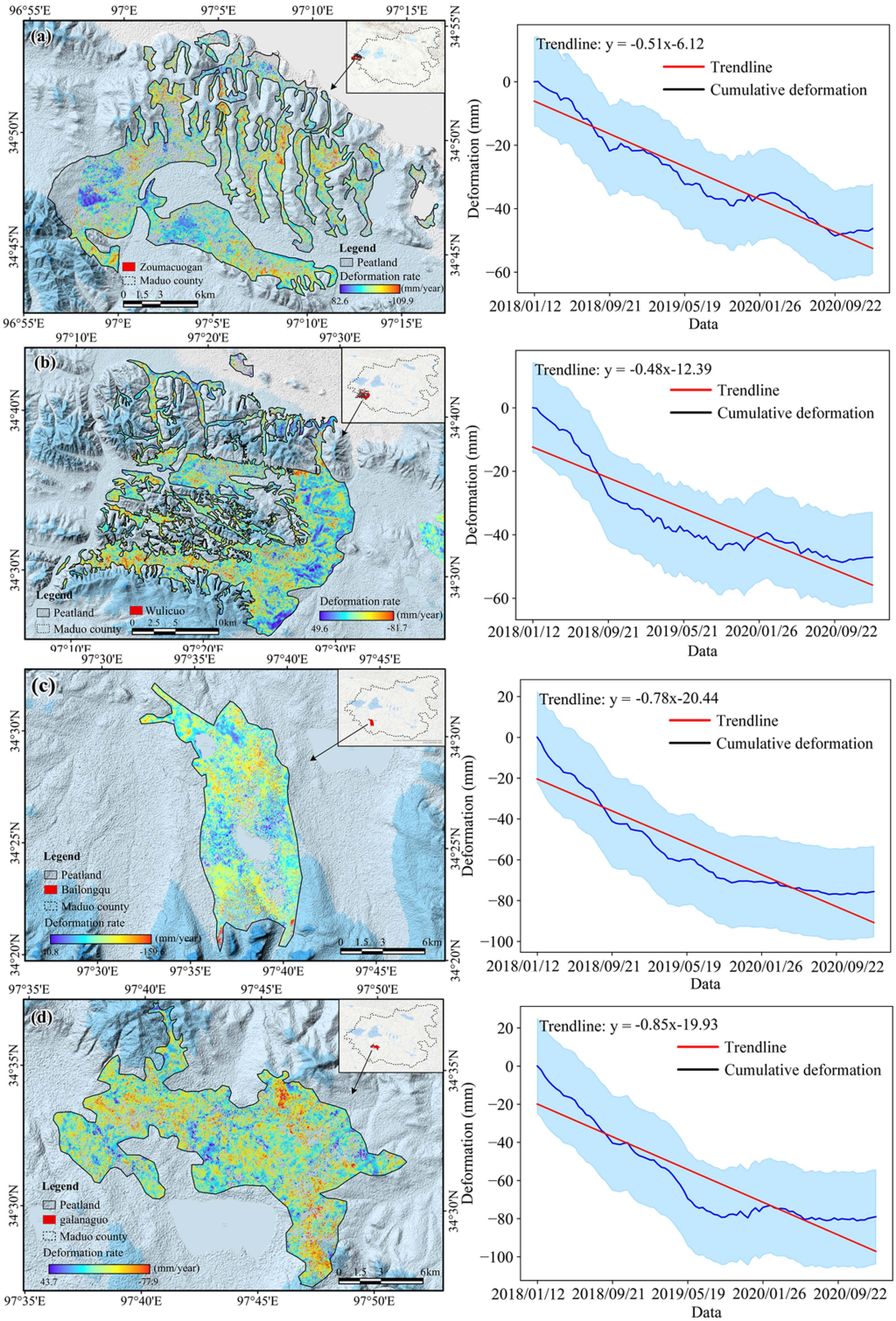

Fig. 11. Time series deformation of typical regional peatland. (a) Zoumacuogan. (b) Walicuo. (c) Bailongqu. (d) Galanaguo. The small maps in the upper right corner (a), (b), (c), and (d) represent the locations of zoumacuogan, walicuo, bailongqu, and galanaguo in Maduo County, respectively.

monitoring results of the PS-InSAR method and SBAS-InSAR method showed that the peatland deformation monitoring results were reliable to a certain extent.

We selected 29 ascending track Sentinel-1A images corresponding to the descending track data from January 12, 2018, to December 29, 2018, and obtained the deformation results of the ascending tracks in the peatland of Madao County by the SBAS-InSAR method. The deformation rate distribution of ascending and descending tracks in the study area in 2018 is shown in Fig. 14. Due to the influence of satellite orbits and data cycles, data is missing in the bottom right corner of the study area, this is displayed as blank in Fig. 14(b). However, this does

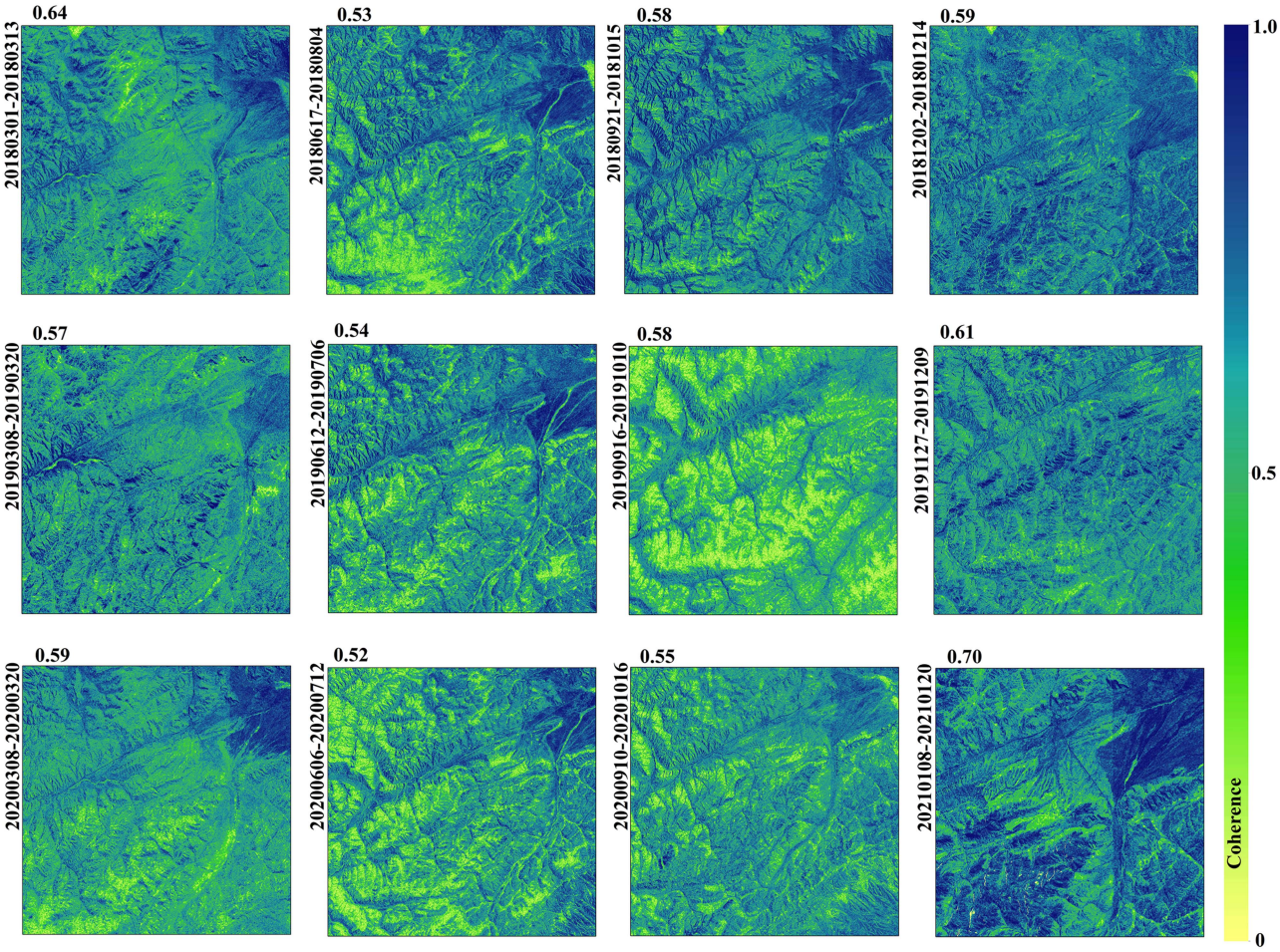

Fig. 12. Coherence plots and coherence coefficients for different periods.

not affect our experimental testing and analysis. As can be seen from Fig. 14, the deformation range of ascending and descending tracks covering the study area is the same distribution, and the deformation rate is similar, indicating that the peatland InSAR deformation results of the ascending and descending tracks in Maduo County have good consistency. We randomly selected the validation area to explore the InSAR results correlation of the ascending and descending tracks. The R2 of the ascending and descending tracks InSAR results in the validation area is 0.63 [see Fig. 14(c)], which further proves that the InSAR results are reliable. However, the ascending tracks InSAR results have a partial incoherence area compared with the descending tracks, as shown by the black dashed line box in Fig. 14(b). Therefore, all the analyses in this article are based on InSAR results of descending tracks.

B. *Drivers of Peatland Surface Deformation*

Most of the peatlands are distributed in high-latitude and high-altitude areas where the seasonal freeze–thaw is a typical surface process [50]. The seasonal freeze-thaw settlement cycle of peatland in Maduo County is mainly affected by meteorological conditions (temperature and precipitation), soil conditions (soil moisture and soil type), and geological conditions (Landform) (see Fig. 15). As temperatures rise, the active layer begins to melt and the peatland slowly subsidence. The degradation of peatland caused by the continuous rise in temperature emits a lot of greenhouse gases, and the subsidence of peatland is intensified. But peatland subsidence has slowed as temperatures have peaked, precipitation and snow melt have increased, and groundwater has been replenished. When the temperature drops, rainfall decreases, and the active layer begins to consolidate, a slight uplift occurs in the peatland. As temperatures continue to decrease and snowfall increases, the active layer freezes completely, leading to an intensification of peatland uplift. Eventually, these results in the formation of a seasonal freeze-thaw settlement cycle.

1) Effect of Precipitation and Temperature on Peatland Surface Deformation: Warming climate accelerates the melting and evaporation of snow, which has some impact on peatlands [21] Therefore, this study calculated the relationship between time series peat topography variables and monthly mean temperature and monthly mean precipitation in the study area. As seen in Fig. 16, since January 2018, with the increasing temperature and precipitation, the consolidated peatland began to melt, and the subsidence of peatland showed an overall increasing trend. However, there was a fluctuation in May 2018, possibly due to a sharp increase in rainfall in May, which accelerated the

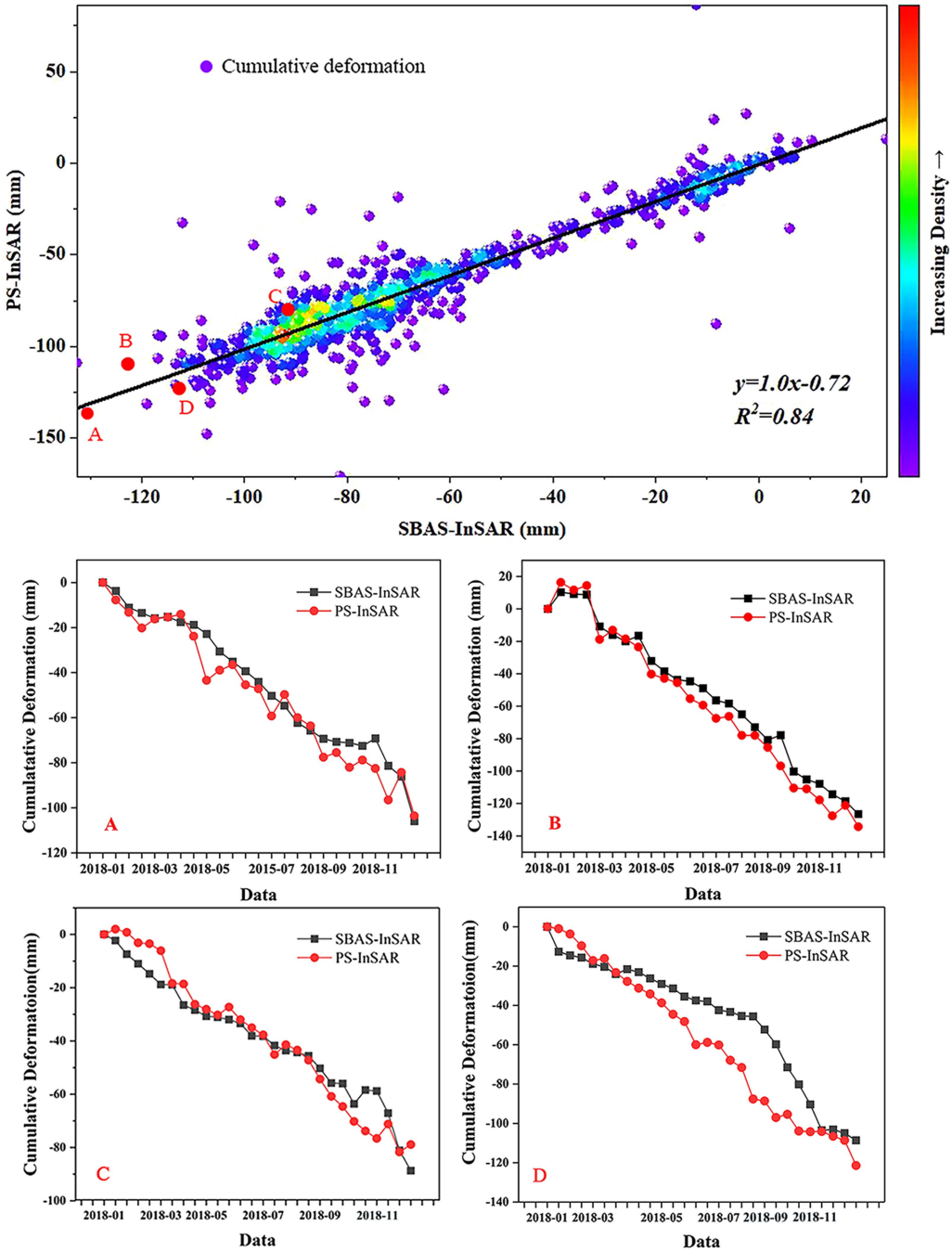

Fig. 13. Correlation of SBAS-InSAR and PS-InSAR results.

growth of swamp vegetation and slowed the rate of peatland decomposition. From June to September 2018, the temperature and precipitation remained unchanged, but the peatland subsidence intensified, and the large evaporation promoted the degradation of peat, the bare peatland surface was oxidized and discharged in the form of CO_2. After September, precipitation decreased sharply, and the peatland subsidence rates slowed down. At this time, the temperature is lower, the evaporation is less, the exposed peatland part begins to consolidate, and the oxidation rate slows down. In November of the same year, precipitation continued to decrease, and the temperature dropped to -13 °C. Most of the peatlands were frozen and expanded, and the frozen soil led to the volume expansion of the peatlands and the surface uplift of the peatlands. In high-altitude regions, due to the stronger diurnal temperature variations in the cold season, the seasonal freeze-thaw processes are characterized by a short period of freeze-up and long shoulder seasons of ground freezing and thawing than their counterparts in high latitudes [50]. In 2019 and 2020, the peatland showed the same pattern of seasonal frezze-thaw settlement with 2018. In April 2019, the precipitation was the highest, while the subsidence accelerated in June, indicating that the influence of precipitation on the surface deformation of peatland has a lag. From the above analysis, it can be seen that precipitation and temperature are important factors causing surface deformation in peatland.

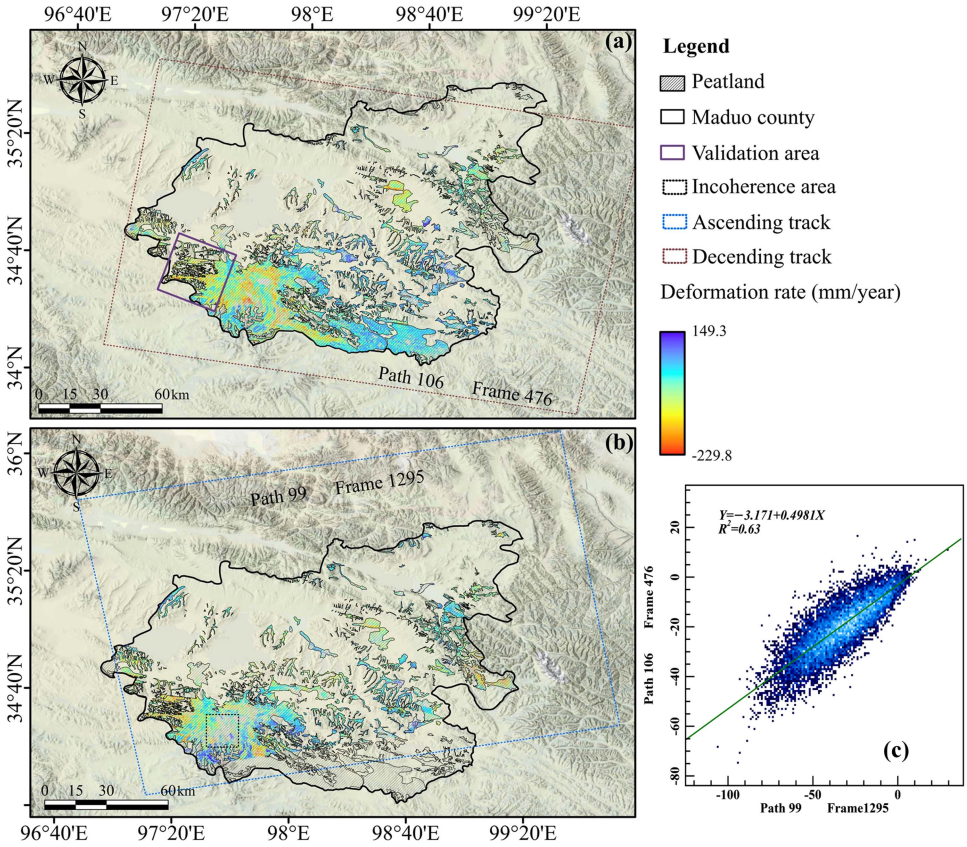

Fig. 14. Deformation rate distribution of the ascending and descending tracks in the peatland of Maduo County in 2018. (a) Deformation rate distribution of descending tracks. (b) Deformation rate distribution of ascending tracks. (c) Deformation rate correlation of the ascending and descending tracks in the validation area.

2) Effect of Soil Condition on Peatland Surface Deformation: Permafrost thaw resulting from climate warming is threatening to release carbon from high-latitude peatlands, soil condition is an important factor affecting the change of peatland surface deformation in high-latitude region [51]. From Fig. 17, soil types in southern Maduo County are Gaelic Leptosols and Mollic Gleysols, Mollic Gleysols development is associated with low-lying topography and is a component of wetland soils with high natural water content, high porosity, and high compressibility. Soil incubation causes soil organic matter to be decomposed by microbial anaerobes, produces organic and inorganic reducing substances and a range of intermediate products [52]. Soil properties are one of the reasons for the severe subsidence of peatlands in southern Maduo County. The middle part is Gelic Leptosols and Gelic Cambisols. The physical properties of permafrost soils are extremely unstable and are particularly strongly affected by temperature. In the process of temperature changes in all seasons, they are often accompanied by freeze-thaw cycles, which reduce the strength of the soil and weaken its ability to resist deformation in the process of freeze-thaw state changes [53], peatland subsidence occurs as a result. The northern part is calcareous daisy soil and simple Yukon salt soil. The northern part is Calcaric Cambisols and Haplic Soionchaks. The formation conditions of the embryonic layer are relatively simple, as long as the soil contains a certain amount of clay particles, under the action of alternating wet and dry, freezing and thawing, soil structure is easily formed [54]. The simpler the formation and structure of the soil, the less resistant it is to damage. Soil structural characteristics in Maduo County and the soil formation processes suggest that soil type is an important factor influencing peatland surface deformation in this region.

The InSAR-estimated peatland surface deformation display annual oscillations ("bog breathing") that are synchronous and positively correlated with the seasonal (dry/wet) evolutions of soil moisture levels [55]. The high soil moisture conditions within the active layer of permafrost zone are not only essential for maintaining the stability of the alpine ecosystem but also form a unique process of ground-air exchange and runoff formation in the permafrost zone through its moisture changes and freezing and thawing [56]. In this study, the effect of soil moisture on peatland deformation was investigated (see Fig. 18). As seen in Fig. 18, soil moisture increased and peatland subsidence intensified. On the one hand, warming led to an increase in the melting depth of the active layer and the melting of subsurface ice near the upper limit of permafrost, resulting in a tendency for the ground to sink [56]. On the other hand, wet mollic gleysols might undergo some degree of deformation and subsidence due to increased contact between particles. From December 2018 to March 2019, soil moisture decreased, while the peatland surface showed a slight uplift. As the temperature decreased, the active layer entered the two-way freezing process, that was, it entered the "zero curtain layer" stage. At this time, the

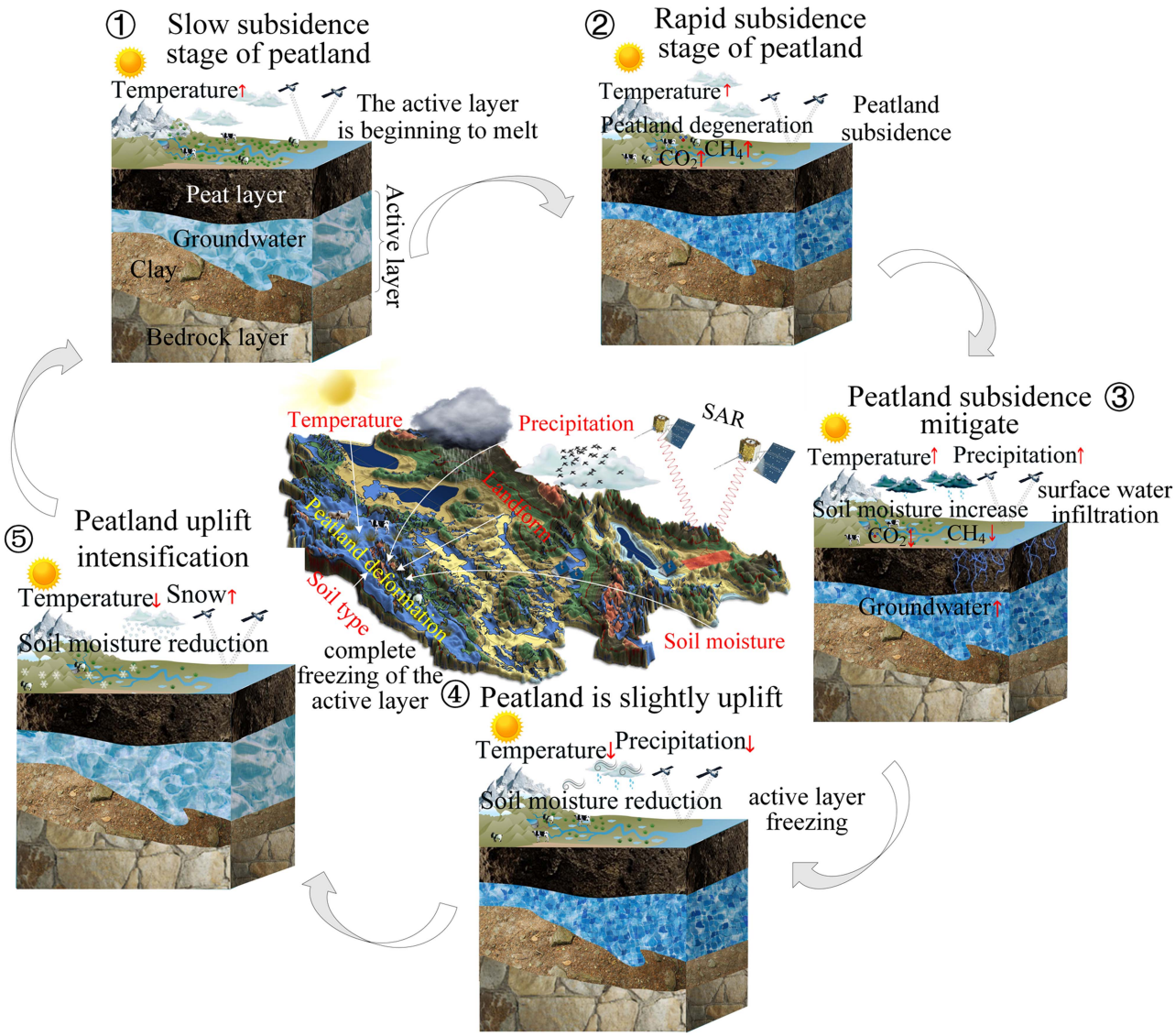

Fig. 15. Monitoring mechanism of peatland deformation and cycle of freeze-thaw settlement in Maduo County.

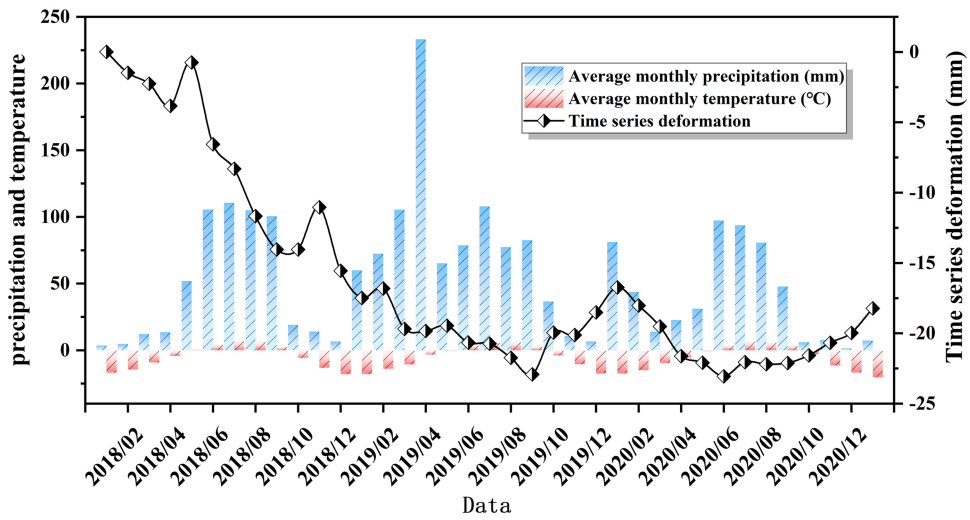

Fig. 16. Effect of temperature and precipitation on peatland surface deformation.

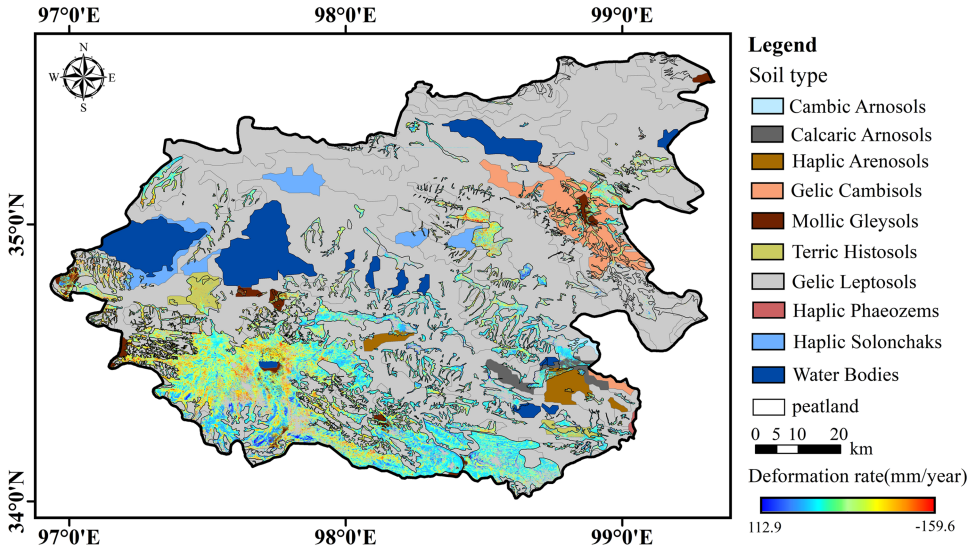

Fig. 17. Influence of soil type on peatland surface deformation.

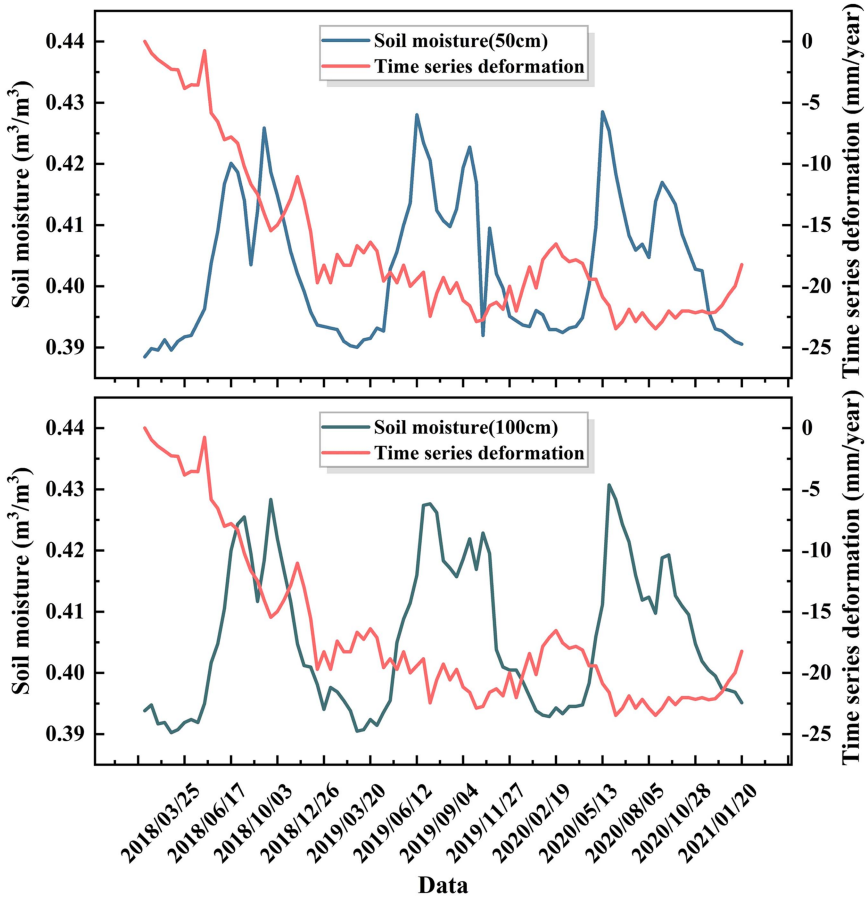

Fig. 18. Relationship between soil moisture and peatland surface deformation.

surface formed a stable freezing layer, the upper freezing front of the melting layer moved rapidly downward, and the water kept migrating and freezing to the freezing front, the surface was mostly uplifting trend [57]. In general, soil moisture of peatland increased and surface subsidence increased. This suggested that seasonal freezing and thawing of the peatland surface occurred with the seasonal freezing and thawing of active layer moisture [57].

3) Effect of Landform on Peatland Surface Deformation: Geological conditions have an impact on the stratigraphic structure and stability of peatlands, and physical properties and stratigraphic sequence of the strata affect the peatland stability

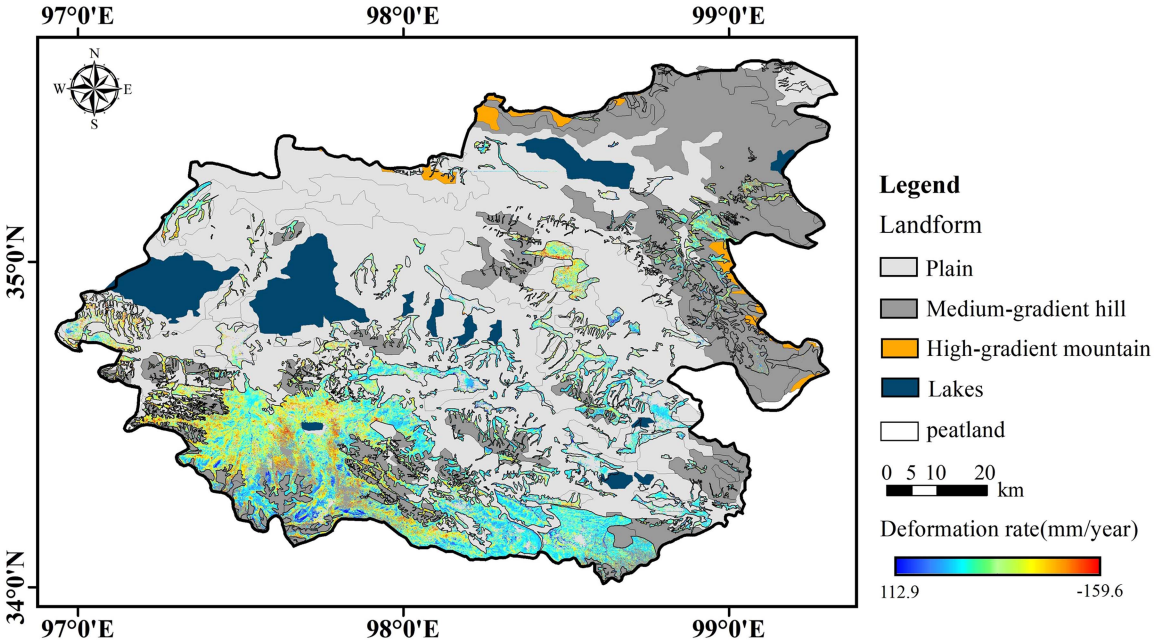

Fig. 19. Influence of landform on peatland deformation.

and soil water supply capacity [58]. The results of peatland surface deformation and distribution of landform types were superimposed (see Fig. 19). As shown in Fig. 18, most peatlands of Maduo County in China are located on medium-slope hills and are peat mound bogs. The central part was mainly plain, and the peatlands were scattered and mostly developed in the lakes and valleys. Only very few peatlands are distributed in the high-gradient mountains in the north. The peatland deformation areas are mainly located in the mid-slope hills in the south and the plains in the west and center.

4) Effect of Combination Factors on Peatland Surface Deformation: Different driving factors in Maduo County of China contribute differently to the distribution of peatland surface deformation. This study further quantitatively analyzed the effects of single impact factor and multiple impact factors on the surface deformation of peatland based on Geo-detector, and the results were shown in Fig. 20. As shown in Fig. 20(a), the contribution of single impact to peatland surface deformation was: mean annual temperature (0.46) > landform type (0.44) = soil type (0.44) > cumulative precipitation (0.31) > soil moisture content (100 cm) (0.20) > soil moisture (50 cm) (0.16). Average annual temperature had the greatest influence on peatland surface deformation, followed by landform type, soil type, and average annual precipitation, while soil moisture at 50 cm and 100 cm below ground explained 20% and 16% of peatland surface deformation, respectively. Soil moisture content had the weakest influence on peatland surface deformation.

The relationship between combination drive factors and peatland surface deformation [see Fig. 20(b)] shows that the q-values of the multifactor detectors were all higher than those of the single-factor detectors, indicating that the explanatory power of the combination factor was greater than that of a single factor. Peatland surface deformation was influenced by multifactor interactions. It can be seen from the q values that mean annual temperature ∩ soil type and mean annual temperature ∩ landform type had the strongest explanatory power, followed by mean annual precipitation ∩ soil type and cumulative precipitation ∩ landform type, and then mean annual temperature ∩ cumulative precipitation, indicating that mean annual temperature ∩ soil type and mean annual temperature ∩ landform had the greatest influence on peatland surface deformation.

The results of the ecological detection, were depicted in Fig. 20(c), illustrated the significant differences in the effects of different combinations of drivers on peatland surface deformation. There were significant differences in the effects of mean monthly temperature and cumulative precipitation and soil moisture on peatland surface deformation, while there are no significant differences in the effects of monthly annual temperature and landform type and soil type on peatland surface deformation. There were significant differences in the effects of precipitation and landform type, soil type, and soil moisture on peatland surface deformation. Landform type and soil type were no significant differences in their effects on peatland surface deformation but differed significantly from soil moisture. Soil type and soil moisture were significant differences in their effects on peatland surface deformation, while there were no significant differences in the effects of soil moisture on peatland surface deformation between 50 and 100 cm below ground. From the above, it can be concluded that the impact of monthly temperature and landform and soil type on peatland surface deformation were consistent. Landform and soil type as geological conditions and their effects on peatland surface deformation were consistent. There were consistent effects of soil moisture on peatland surface deformation between 50 and 100 cm below ground.

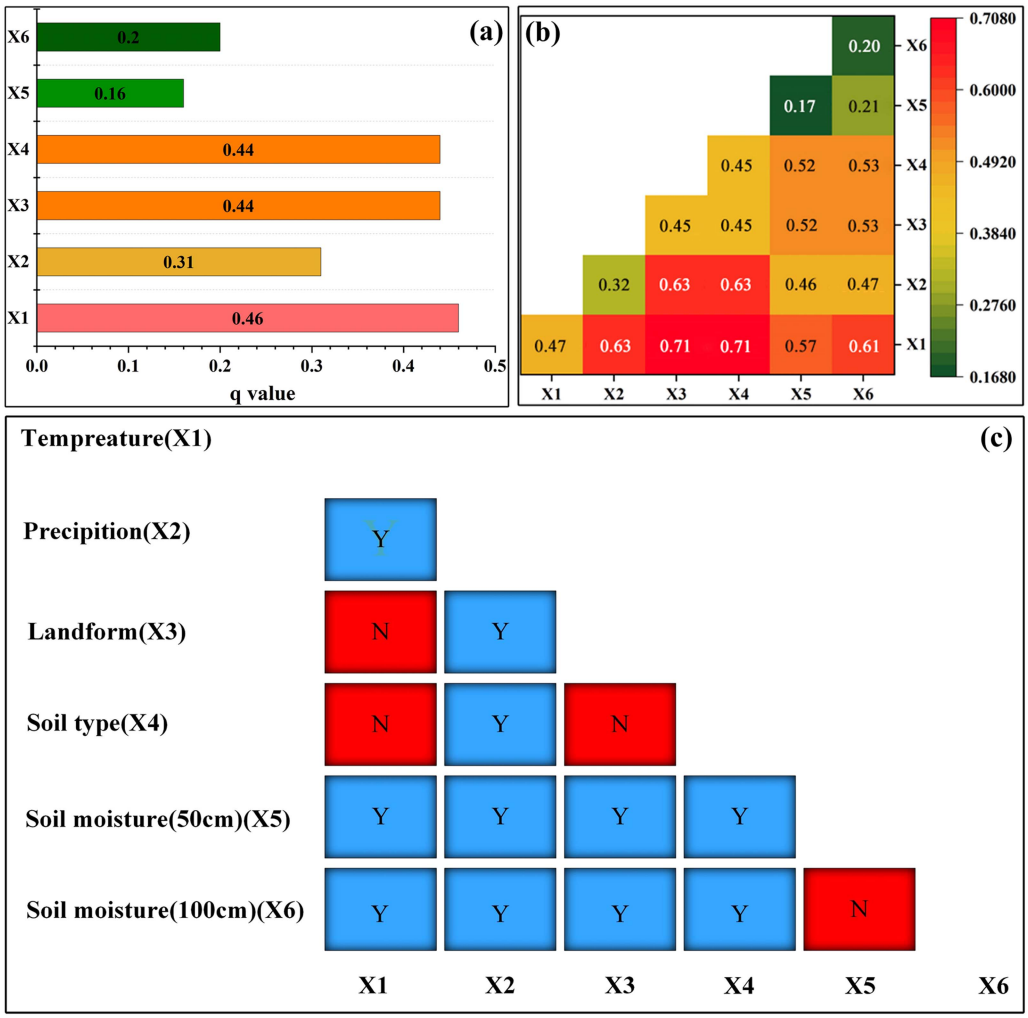

Fig. 20. Results of peatland deformation driver detection. (a) Single-factor driving importance distribution. (b) Multifactor interaction detection results. (c) Combined driving effect differences.

C. Shortcomings and Prospects

This study demonstrated the potential of time-series InSAR technology for peatland monitoring in the alpine region of China, but we also need a rigorous accuracy verification method to understand the difference between the measured and true values. In the future, we consider using GNSS data validation or field measurements to improve the validation work to increase the reliability of monitoring results. In this study, the driving mechanisms of peatland surface deformation in Maduo County of China were investigated based on meteorological data, geological data, and soil moisture data, and the main factors affecting peatlands were quantified. In the future, we consider adding more driving factors to explore the mechanisms driving the surface deformation of peatlands, such as GL changes and land use changes.

V. Conclusion

Surface deformation of peatlands in Maduo County of China during 2018–2021 was monitored based on Sentinel-1A data, and the results of peatland InSAR surface deformation were evaluated by internal validation and cross-validation. Results of peatland InSAR surface deformation were reliable. The peatland surface deformation rate in Maduo County of China was -159 to 112 mm/year during 2018–2021, and peatland surface deformation showed seasonal freezing and thawing. The overall subsidence rate slowed down year by year. Total of 39.2% of the peatlands occurred surface subsidence. Among them, Zoumacuogan, Walicuo, Letongma, Bailongqu, Galanaguo, Maliecuo, Gaerlawangzang, Dalong, and Duoqu subsidence were more serious. The development of peatlands and surface deformation differed under different topographic conditions, peatlands were stable at high elevations and high slopes, while peatlands were vulnerable to disturbance at low elevations and low slopes. Mean annual temperature, landform type, and soil type mainly contributed to peatland surface deformation.

References

[1] W. Song et al., "Methane emissions from an alpine wetland on the Tibetan Plateau: Neglected but vital contribution of the nongrowing season," *J. Geophys. Res., Biogeosci.*, vol. 120, pp. 1475–1490, 2015.

[2] C. Lin et al., "Effects of degradation succession of alpine wetland on soil organic carbon and total nitrogen in the Yellow River source zone, West China," *J. Mountain Sci.*, vol. 18, pp. 694–705, 2021.

[3] H. Yin, H. Zhu, F. Lv, and R. Wang, "A study on the spatial and temporal distribution pattern of peat resources in China based on CPGIS," in *Proc. Symp. Land Change Sci. Ecological Construction*, 2004, pp. 547–551.

[4] T. Ma et al., "Alpine wetland evolution and their response to climate change in the yellow-river-source national park from 2000 to 2020," *Water*, vol. 14, 2022, Art. no. 2351.

[5] H. Song, Y. Zhang, H. Gao, Y. Guo, and S. Li, "Plateau wetlands, an indispensible habitat for the black-necked crane (Grus nigricollis) a review," *Wetlands*, vol. 4, pp. 629–639, 2014.

[6] X. Li, J. Zhang, and J. Gao, "A topographic perspective on the propensity for degradation of plateau swampy meadows in Maduo County, West China," *Land*, vol. 12, 2023, Art. no. 80.

[7] W. Ma, A. Alhassan, Y. Wang, G. Li, H. Wang, and J. Zhao, "Greenhouse gas emissions as influenced by wetland vegetation degradation along a moisture gradient on the eastern Qinghai-Tibet Plateau of North-West China," *Nutr. Cycling Agroecosyst.*, vol. 112, pp. 335–354, 2018.

[8] L. Zhao et al., "Seasonal variations in carbon dioxide exchange in an alpine wetland meadow on the Qinghai-Tibetan Plateau," *Biogeosciences*, vol. 7, pp. 1207–1221, 2010.

[9] X. Li, J. Zhang, and J. Gao, "A topographic perspective on the propensity for degradation of plateau swampy meadows in Maduo County, West China," *Land*, vol. 12, 2023, Art. no. 80.

[10] X. Li, Z. Xue, and J. Gao, "Dynamic changes of plateau wetlands in Madou County, the Yellow River source zone of China: 1990–2013," *Wetlands*, vol. 36, pp. 299–310, 2016.

[11] J. Gao, X. Li, G. Brierley, A. Cheung, and Y. Yang, "Geomorphic-centered classification of wetlands on the Qinghai-Tibet Plateau, Western China," *J. Mountain Sci.*, vol. 10, pp. 632–642, 2013.

[12] J. Gao, "Wetland and its degradation in the Yellow River Source Zone," in *Proc. Landscape Ecosystem Diversity, Dyn. Manage. Yellow River Source Zone*, 2016, pp. 209–232.

[13] C. Evans et al., "Rates and spatial variability of peat subsidence in Acacia plantation and forest landscapes in Sumatra, Indonesia," *Geoderma*, vol. 338, pp. 410–421, 2019.

[14] B. Dahdal, *The Use of Interferometric Spaceborne Radar and GIS to Measure Ground Subsidence in Peat Soils in Indonesia*. Leicester, U.K.: Univ. Leicester, 2011.

[15] Z. Zhou, *The Applications of InSAR Time Series Analysis for Monitoring Long-Term Surface Change in Peatlands*. Glasgow, U.K.: Univ. Glasgow, 2013.

[16] A. Hrysiewicz, E. P. Holohan, S. Donohue, and H. Cushnan, "SAR and InSAR data linked to soil moisture changes on a temperate raised peatland subjected to a wildfire," *Remote Sens. Environ.*, vol. 291, 2023, Art. no. 113516.

[17] D. Umarhadi et al., "Tropical peat subsidence rates are related to decadal LULC changes: Insights from InSAR analysis," *Sci. Total Environ.*, vol. 816, 2022, Art. no. 151561.

[18] T. Tampuu, J. Praks, F. De Zan, M. Kohv, and A. Kull, "Relationship between ground levelling measurements and radar satellite interferometric estimates of bog breathing in ombrotrophic northern bogs," *Mires Peat*, vol. 29, 2023, Art. no. 17.

[19] S. Valman et al., "Permafrost degradation of peatlands in northern Sweden," *Cryosphere Discuss.*, pp. 1–20, 2023.

[20] B. Zhou, Z. Li, Y. You, and H. Lu, "Distribution and spatial differences of peatlands in the source region of the yellow river in 2015," *Wetland Sci.*, vol. 19, pp. 543–550, 2021.

[21] J. Gao, X. Li, and G. Brierley, "Topographic influence on wetland distribution and change in Maduo County, Qinghai-Tibet Plateau, China," *J. Mountain Sci.*, vol. 9, pp. 362–371, 2012.

[22] Y. Chen, L. Zhang, Y. He, W. Wang, and Y. Tang, "Research on the relationship between land deformation and land use types in Lanzhou new district," *Sci. Surveying Mapping*, vol. 46, pp. 80–89, 2021.

[23] W. Yang, Y. He, L. Zhang, W. Wang, Y. Chen, and Y. Chen, "InSAR monitoring of the three-dimensional surface deformation in Jinchan mining aera, Gansu Province," *Remote Sens. Natural Resour.*, vol. 34, pp. 177–188, 2022.

[24] Z. Bai, B. Wang, G. Jing, Q. Xu, H. Zhang, and H. Liu, "Applicability analysis of ground deformation monitoring in mining area by Sentinel−1A data," *Remote Sens. Land Resour.*, vol. 31, pp. 210–217, 2019.

[25] Y. He et al., "An integrated neural network method for landslide susceptibility assessment based on time-series InSAR deformation dynamic features," *Int. J. Digit. Earth*, vol. 17, no. 1, 2024, Art. no. 2295408.

[26] C. Yu, Z. Li, N. T. Penna, and P. Crippa, "Generic atmospheric correction model for interferometric synthetic aperture radar observations," *J. Geophys. Res., Solid Earth*, vol. 123, pp. 9202–9222, 2018.

[27] B. Liu, "Actual livestock carrying capacity estimation product in Qinghai-Tibet Plateau (2000-2019)," National Tibetan Plateau Data Center. 2021. [Online]. Available: https://doi.org/10.11888/Ecolo.tpdc.271512

[28] S. Peng, Y. Ding, W. Liu, and Z. Li, "1 km monthly temperature and precipitation dataset for China from 1901 to 2017," *Earth Syst. Sci. Data*, vol. 11, pp. 1931–1946, 2019.

[29] K. Dijkshoorn, V. van Engelen, and J. Huting, "Soil and landform properties for LADA partner countries," ISRIC Rep., vol. 6, 2008.

[30] Q. Li et al., "A 1 km daily soil moisture dataset over China using in situ measurement and machine learning," *Earth Syst. Sci. Data*, vol. 14, pp. 5267–5286, 2022a.

[31] P. Berardino, G. Fornaro, R. Lanari, and E. Sansosti, "A new algorithm for surface deformation monitoring based on small baseline differential SAR interferograms," *IEEE Trans. Geosci. Remote Sens.*, vol. 40, no. 11, pp. 2375–2383, Nov. 2002.

[32] S. Yao et al., "A convLSTM neural network model for spatiotemporal prediction of mining area surface deformation based on SBAS-InSAR monitoring data," *IEEE Trans. Geosci. Remote Sens.*, vol. 61, 2023, Art. no. 5201722.

[33] Y. He et al., "An identification method of potential landslide zones using InSAR data and landslide susceptibility," *Geomatics, Natural Hazards Risk*, vol. 14, 2023, Art. no. 2185120.

[34] Y. He et al., "Time-series analysis and prediction of surface deformation in the Jinchuan mining area, Gansu Province, by using InSAR and CNN–PhLSTM network," *IEEE J. Sel. Topics Appl. Earth Observ. Remote Sens.*, vol. 15, pp. 6732–6751, 2022.

[35] A. Ferretti, C. Prati, and F. Rocca, "Permanent scatterers in SAR interferometry," *IEEE Trans. Geosci. Remote Sens.*, vol. 39, no. 1, pp. 8–20, Jan. 2001.

[36] Y. Chen et al., "Prediction of InSAR deformation time-series using a long short-term memory neural network," *Int. J. Remote Sens.*, vol. 42, pp. 6919–6942, 2021.

[37] J. Wang and C. Xu, "Geodetector: Principle and prospective," *Acta Geogr. Sinica*, vol. 72, pp. 116–134, 2017.

[38] W. Wang, Y. He, L. Zhang, Y. Chen, L. Qiu, and H. Pu, "Analysis of surface deformation and driving forces in Lanzhou," *Open Geosci.*, vol. 12, pp. 1127–1145, 2020.

[39] D. Millar, D. Cooper, K. Dwire, R. Hubbard, and J. von Fischer, "Mountain peatlands range from CO_2 sinks at high elevations to sources at low elevations: Implications for a changing climate," *Ecosystems*, vol. 20, pp. 416–432, 2017.

[40] J. Urbina and J. Benavides, "Simulated small scale disturbances increase decomposition rates and facilitates invasive species encroachment in a high elevation tropical Andean peatland," *Biotropica*, vol. 47, pp. 143–151, 2015.

[41] I. Olorunfemi, A. Komolafe, J. Fasinmirin, A. Olufayo, and S. Akande, "A GIS-based assessment of the potential soil erosion and flood hazard zones in Ekiti State, Southwestern Nigeria using integrated RUSLE and HAND models," *Catena*, vol. 194, 2020, Art. no. 104725.

[42] B. Makaske and G. Maas, "Different hydrological controls causing variable rates of holocene peat growth in a lowland valley system, north-eastern Netherlands; implications for valley peatland restoration," *Holocene*, vol. 33, pp. 960–974, 2023.

[43] J. Sun, A. Gallego-Sala, and Z. Yu, "Topographic and climatic controls of peatland distribution on the Tibetan Plateau," *Sci. Rep.*, vol. 13, 2023, Art. no. 14811.

[44] Y. Li, Z. Yu, M. Wang, H. Li, S. Wang, and J. Sun, "Control of local topography and surface patterning on the formation and stability of a slope permafrost peatland at 4800-m elevation on the central Qinghai-Tibetan Plateau," in *Proc. AGU Fall Meeting Abstr.*, 2022, Art. no. B31A-01.

[45] B. Gao et al., "Landslide risk evaluation in Shenzhen based on stacking ensemble learning and InSAR," *IEEE J. Sel. Topics Appl. Earth Observ. Remote Sens.*, vol. 16, pp. 1–18, 2023.

[46] X. He, Y. He, L. Zhang, Y. Chen, H. Pu, and B. Chen, "Spatio-temporal analysis of land subsidence in Beijing plain based on InSAR and PCA," *Spectrosc. Spectral Anal.*, vol. 42, pp. 2315–2324, 2022.

[47] X. Yu, D. Xue, and F. Chen, "Analysis of influence of vegetation coverage and slope on SAR interferometric coherence," *Mountain Res.*, vol. 38, pp. 926–934, 2020.

[48] K. Dai et al., "Monitoring highway stability in permafrost regions with X-band temporary scatterers stacking InSAR," *Sensors*, vol. 18, 2018, Art. no. 1876.

[49] Y. Chen et al., "Surface deformation prediction based on TS-InSAR technology and long short-term memory networks," *Nat. Remote Sens. Bull.*, vol. 26, pp. 1326–1341, 2022.
[50] Z. Yang, D. Zhu, L. Liu, X. Liu, and H. Chen, "The effects of freeze–thaw cycles on methane emissions from peat soils of a high-altitude peatland," *Front. Earth Sci.*, vol. 10, 2022, Art. no. 850220.
[51] B. De la Barreda-Bautista et al., "Towards a monitoring approach for understanding permafrost degradation and linked subsidence in arctic peatlands," *Remote Sens.*, vol. 14, 2022, Art. no. 444.
[52] J. Ma, Y. Lu, M. Zhao, and S. Pan, "Development trend and improvement utilization of submerged swampy soil in the middle Yangtze River plain lake area," *Soils*, no. 1, pp. 1–5, 1997.
[53] Z. Feng, "Experimental study on the mechanical properties of frozen peat soil," *High Speed Railway Technol.*, vol. 11, pp. 28–31, 2020.
[54] F. Zhang and L. Zhang, "Soil erosion is the main influence process of the widely distributed cambosols and primosols," *J. China Agricultural Univ.*, vol. 27, pp. 1–13, 2022.
[55] A. Hrysiewicz, E. Holohan, S. Donohue, and H. Cushnan, "SAR and InSAR data linked to soil moisture changes on a temperate raised peatland subjected to a wildfire," *Remote Sens. Environ.*, vol. 291, 2023, Art. no. 113516.
[56] Z. Li et al., "Analysis of soil moisture content in the active layer in the permafrost region of the Tuotuo River source in frozen season," *J. Glaciology Geopcrylogy*, vol. 44, pp. 56–68, 2022.
[57] S. Liu et al., "Application of InSAR technology to monitor deformation in permafrost areas," *J. Glaciology Geopcrylogy*, vol. 43, pp. 964–975, 2021.
[58] M. Omar et al., "Peatlands in Southeast Asia: A comprehensive geological review," *Earth Sci. Rev.*, vol. 232, 2022, Art. no. 104149.

Yaoxiang Liu received the B.E. degree in remote sensing science and technology from the Lanzhou Jiaotong University, Lanzhou, China, in 2019, where he is currently working toward the M.S. degree at the Faculty of Geomatics, studying the identification of peatlands and the study of long time series changes in the source region of the Yellow River in China.

His research interests include InSAR data processing technology, machine learning, and remote sensing image information extraction.

Yi He received the B.S. degree in geographic information system from Lanzhou Jiaotong University, Lanzhou, China, in 2011, and the Ph.D. degree in earth system science from Lanzhou University, Lanzhou, China, in 2016.

He is a Postdoctoral Researcher with the School of Environment and Municipal Engineering, Lanzhou Jiaotong University. He is currently a Professor with the Faculty of Geomatics, Lanzhou Jiaotong University. His research interests include disaster remote sensing, ecological remote sensing, image processing, and time series InSAR prediction based on deep learning.

Wang Yang received the M.S. degree in surveying and mapping, in 2023, from Lanzhou Jiaotong University, Lanzhou, China, where he is currently working toward the Ph.D. degree in surveying and mapping with the Faculty of Geomatics. His research interests include InSAR data processing technology, machine learning, and remote sensing image information extraction.

Lifeng Zhang received the M.S. degree in cartography and geographic information system and the Ph.D. degree in environmental science and engineering from Lanzhou Jiaotong University, Lanzhou, China, in 2010 and 2017, respectively.

He is a Professor with Lanzhou Jiaotong University. His research interests include ecological environment remote sensing monitoring, visualized analysis, and analysis of land use change.